

Review

# High-Entropy Alloy Coatings Deposited by Thermal Spraying: A Review of Strengthening Mechanisms, Performance Assessments and Perspectives on Future Applications

Rakesh Bhaskaran Nair <sup>1,2,\*</sup>, Raunak Supekar <sup>1,†</sup>, Seyyed Morteza Javid <sup>3</sup>, Wandong Wang <sup>4</sup>, Yu Zou <sup>4</sup>, André McDonald <sup>2</sup>, Javad Mostaghimi <sup>3</sup> and Pantcho Stoyanov <sup>5,\*</sup>

<sup>1</sup> Department of Mechanical, Industrial and Aerospace Engineering, Concordia University, Montreal, QC H3G 2W1, Canada

<sup>2</sup> Department of Mechanical Engineering, University of Alberta, Edmonton, AB T6G 1H9, Canada

<sup>3</sup> Department of Mechanical and Industrial Engineering, University of Toronto, Toronto, ON M5S 3G8, Canada

<sup>4</sup> Department of Material Science and Engineering, University of Toronto, Toronto, ON M5S 3G8, Canada

<sup>5</sup> Department of Chemical and Materials Engineering, Concordia University, Montreal, QC H3G 2W1, Canada

\* Correspondence: rsaraswa@ualberta.ca (R.B.N.); pantcho.stoyanov@concordia.ca (P.S.)

† These authors contributed equally to this work.



**Citation:** Bhaskaran Nair, R.; Supekar, R.; Morteza Javid, S.; Wang, W.; Zou, Y.; McDonald, A.; Mostaghimi, J.; Stoyanov, P. High-Entropy Alloy Coatings Deposited by Thermal Spraying: A Review of Strengthening Mechanisms, Performance Assessments and Perspectives on Future Applications. *Metals* **2023**, *13*, 579. <https://doi.org/10.3390/met13030579>

Academic Editor: Robert B. Heimann

Received: 23 January 2023

Revised: 2 March 2023

Accepted: 3 March 2023

Published: 13 March 2023



**Copyright:** © 2023 by the authors. Licensee MDPI, Basel, Switzerland. This article is an open access article distributed under the terms and conditions of the Creative Commons Attribution (CC BY) license (<https://creativecommons.org/licenses/by/4.0/>).

**Abstract:** Thermal spray deposition techniques have been well-established, owing to their flexibility in addressing degradation due to wear and corrosion issues faced due to extreme environmental conditions. With the adoption of these techniques, a broad spectrum of industries is experiencing continuous improvement in resolving these issues. To increase industrial-level implementation, state-of-the-art advanced materials are required. High-entropy alloys (HEAs) have recently gained considerable attention within the scientific community as advanced materials, mainly due to their exceptional properties and desirable microstructural features. Unlike traditional material systems, high-entropy alloys are composed of multi-component elements (at least five elements) with equimolar or nearly equimolar concentrations. This allows for a stable microstructure that is associated with high configurational entropy. This review article provides a critical assessment of different strengthening mechanisms observed in various high-entropy alloys developed by means of deposition techniques. The wear, corrosion, and oxidation responses of these alloys are reviewed in detail and correlated to microstructural and mechanical properties and behavior. In addition, the review focused on material design principles for developing next-generation HEAs that can significantly benefit the aerospace, marine, oil and gas, nuclear sector, etc. Despite having shown exceptional mechanical properties, the article describes the need to further evaluate the tribological behavior of these HEAs in order to show proof-of-concept perspectives for several industrial applications in extreme environments.

**Keywords:** aerospace materials; high-entropy alloys; microstructure; phase formations; strengthening mechanisms; tribology

## 1. Introduction

Traditional alloy design strategies generally consist of combining one or two principal elements with a few minor elements in order to achieve the desired microstructural features and mechanical properties. However, these strategies restrict the plausible number of combinations for developing advanced alloys since most of the dominant elements would be either iron, aluminum, or nickel. A paradigm shift in the alloy design concept occurred in 2004 when Cantor et al. [1] and Yeh et al. [2] developed advanced metallic alloys by mixing multiple elements without differentiating solvent and solute atoms. Cantor et al. [1] reported this design concept as “multi-component alloy systems”, whereas the term “high-entropy alloys (HEAs)” was derived from the pioneering work of Yeh et al. [2].

Since then, the term HEAs has become popular among the scientific communities, and researchers had put significant efforts into investigating the microstructural features and phase formations that formed for different HEAs, as well as their impact on different industrial applications, including wear and corrosion. Studies have shown that the HEAs possess unique microstructural characteristics that result in the stabilization of solid solution structures with adjustable properties depending upon the chemical compositions used.

High-entropy alloys are defined based on chemical compositions—containing five or more principal elements with equimolar concentrations or close to equimolar concentrations, unlike the traditional alloy design strategies [1,2]. The concentrations of major elements range between 5 at% and 35 at%, with the possibility of adding minor elements less than 5 at% [3]. It has been reported that the HEAs possess inherently high configurational entropy ( $>1.5R$ , where  $R$  is the ideal gas constant) compared to traditional alloys ( $<1.0R$ ) (Figure 1). Thus, a new definition for HEAs arose based on high configurational entropy per mole, where the alloy should exhibit a configurational entropy greater than  $1.5R$ . In the field of statistical mechanics, the “ $1.5R$ ” notation is closely linked to the concept of entropy. Entropy refers to the total number of possible configurations or arrangements that a system can hence assume the possible number of configurations is considerably higher for HEAs than those of binary alloys and/or ternary alloys. If the configurational entropy values are less than  $1.5R$ , the alloys are classified as medium entropy systems (see Figure 1).

| Low Entropy Alloy  | Medium Entropy Alloy                  | High Entropy Alloy   |
|--|---------------------------------------|--|
| $\Delta S_{Conf} \leq 1.0R$  | $1.0R \leq \Delta S_{Conf} \leq 1.5R$ | $\Delta S_{Conf} \geq 1.5R$  |
| One or two dominant elements. Formation of solid solution and/or compounds | Two to four dominant elements         | Five or more dominant elements. Single phase solid solution phase formations (FCC/BCC or both) |

**Figure 1.** Differences between low-, medium-, and high-entropy alloys based on their configurational entropy.

However, it has been argued that the high configurational entropy effect bestows the single-phase solid solution structure (disordered or partially ordered) for HEAs, either in the form of face-centered cubic (FCC), body-centered cubic (BCC), or the combination. The contribution of enthalpy of mixing and the high configurational entropy is key in reducing the Gibbs free energy of the system for obtaining the single-phase structure, as per Equation (1).

$$\Delta G = \Delta H_{mix} - T\Delta H_{conf} \quad (1)$$

where  $\Delta G$  is Gibbs free energy,  $T$  is the temperature in Kelvin,  $\Delta H_{mix}$  and  $\Delta H_{conf}$  represents mixing enthalpy and configuration entropy. It has been reported that the reduction in Gibbs free energy facilitates the disordered solid solution microstructure because of the spontaneous reaction that occurred at high temperatures resulting from the high configurational entropy. Debates on the formation of intermetallic compounds (i.e., B2,  $\sigma$  phases) in HEAs are still going on. However, the combination of disordered and ordered structures may significantly play a crucial role in desirable properties based on the selection of compositions. Besides, other core effects such as sluggish diffusion, lattice distortion, and cocktail effects also favor HEAs with desired properties than traditional alloys [3]. HEAs also go by the names such as complex concentrated alloys [4], compositionally complex alloys [4], multi-component alloys [1], and baseless alloys [5].

Owing to the compositionally complex structures, HEAs possess superior strength, excellent fracture toughness, fatigue strength, high-temperature oxidation, and corrosion resistance, as well as improved wear resistance [3,6–8]. While earlier studies focused mainly on understanding the mechanical behavior of arc-melted HEAs, the advancement of HEA coatings by means of thermal spray techniques has recently gained more attention. Indeed, with the advent of these advanced materials, there is a demand for the development of time-efficient, reliable, and environmentally friendly deposition techniques that benefits the HEAs in controlling degradation-related problems. As shown in Figure 2, the demand for HEAs by means of thermal spraying technologies has been increasing in accordance with the number of research publications per year since 2016. Thermal spraying technologies are well-established in many industrial sectors for developing layers due to their ability to deposit a wide range of feedstocks to protect industrial components against extreme environments caused by wear, corrosion, and oxidation [9–11]. Thermal spraying is a deposition process in which a high-temperature heat source is used to melt the starting material, either in the form of powder particles or solid wires, and the heated particles (molten or semi-molten) are accelerated towards the target substrate with the aid of a propellant gas to produce thick coatings in the form of continuous splats [11]. Thus far, air plasma spraying (APS), high-velocity oxy-fuel (HVOF), high-velocity air-fuel (HVOF), flame spraying (FS), and cold spraying (CS) was employed to study the HEA coatings.

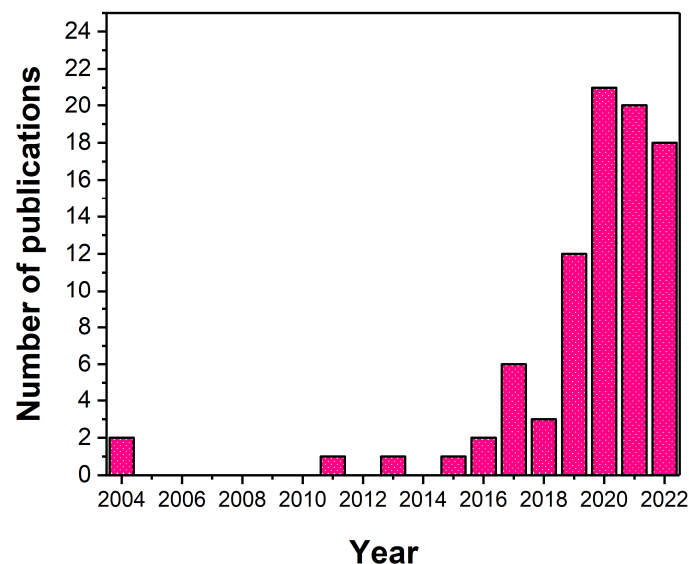


**Figure 2.** The number of publications of thermal spray high-entropy alloy coatings per year until December 2022 (exported with Scopus analysis tool).

Although thermal spray technologies have the advantage of producing thick coatings (typically ranging from 100  $\mu\text{m}$  to a few mm in thickness) compared to thin film deposition techniques such as vacuum arc deposition and magnetron sputtering, the oxide contaminations, voids, and heterogenous microstructure are the major shortcomings for thermal spraying methods. The occurrence of these oxides, porosities, and phase transitions can be eliminated by employing solid-state depositions such as cold spraying and high-velocity air fuel (HVOF) technologies. Since cold spraying and HVOF techniques are new in the field for producing HEA coatings, there are limited literature available that focuses on microstructure and mechanical properties. In contrast to solid-state deposition techniques, high-temperature depositions such as high-velocity oxy-fuel (HVOF) and atmospheric plasma spraying (APS) so far, are widely investigated for producing the HEA coatings for different applications such as wear, corrosion, and oxidation.

With the increasing demand for HEA materials and coatings, the synthesis of feedstock needs to be optimized since it plays a vital role in producing coatings with negligible microstructural inhomogeneities. This will pave the way for desirable mechanical properties, such as strength, hardness, and toughness, which in turn, provide better industrial sustainability. Nevertheless, the quality and characteristics of the feedstock powders are determined by the fabrication routes, which include particle size and morphology, homogeneity, powder yield, and flowability [12,13]. HEAs possess the potential to be utilized as coatings, thereby increasing their applicability in various industrial sectors, thanks to their ability to consume less feedstock and deposit onto intricate components in comparison to their bulk alloy counterparts. For comprehensive information on HEA coatings, Meghwal et al. [12] provide an in-depth review covering diverse aspects of these coatings, including feedstock preparations, different HEA coating systems, and their microstructures. While these techniques are versatile, research on thermal-sprayed HEA coatings, and their impact on strengthening mechanisms and tribological aspects, remains limited and not entirely understood. This review article, therefore, critically assesses the microstructure and strengthening mechanisms of numerous HEA coatings deposited using different thermal spraying technologies. It also provides a detailed review and discussion of the wear, corrosion, and oxidation responses of various HEAs. Furthermore, the article reports on the feasibility of next-generation high-entropy alloys, highlighting the development of high-performance coating materials and their potential benefits for sustainable industrial futures.

## 2. Preparation of HEA Feedstock

Many researchers have been devoted to fabricating HEA feedstocks for the thermal spraying by means of mechanical blending, mechanical alloying, gas atomization, mechanical milling of as-casted HEAs, and, more recently, radio frequency inductively coupled plasma (RF-ICP). The properties of the coatings strongly depend on the feedstock morphologies. Mechanical blending involves the mixing of each elemental powder without any bonding formation, and the features of powder particles remain unchanged [14,15]. Nevertheless, the feedstock preparation using mechanical blending is not recommended, given that these feedstocks do not contribute to quality microstructure and desired properties. For instance, Lobel et al. [14] investigated the impact of three feedstocks prepared by mechanical blending, mechanical alloying, and gas atomization of AlCoCrFeNiTi HEAs and deposited on S235 steel substrates via the atmospheric plasma spray system. Figure 3 shows the microstructure for all three HEA coatings prepared by different feedstock routes. Among these HEA coatings, the gas-atomized showed homogeneous microstructure with fewer defects compared to those of mechanically blended and mechanically alloyed powder-based coatings. The authors also reported that the hardness showed a significant difference in the values for the coatings prepared by three different feedstocks. The highest average hardness (Vickers micro-hardness test) was found for the gas atomized powder deposited coatings, with around  $5.8 \pm 0.8$  GPa, followed by mechanical alloyed and mechanical blended deposited coatings of approximately  $4.6 \pm 1.1$  GPa and  $3.4 \pm 0.9$  GPa, respectively. This was most probably related to the formation of a homogeneous microstructure for the gas-atomized powder-deposited coatings (see Figure 3). The mechanically blended powders showcase the presence of titanium and nickel contents along with BCC and FCC phases, highlighting the inappropriate formation of alloy microstructure compared to the coatings deposited with gas-atomized powders.

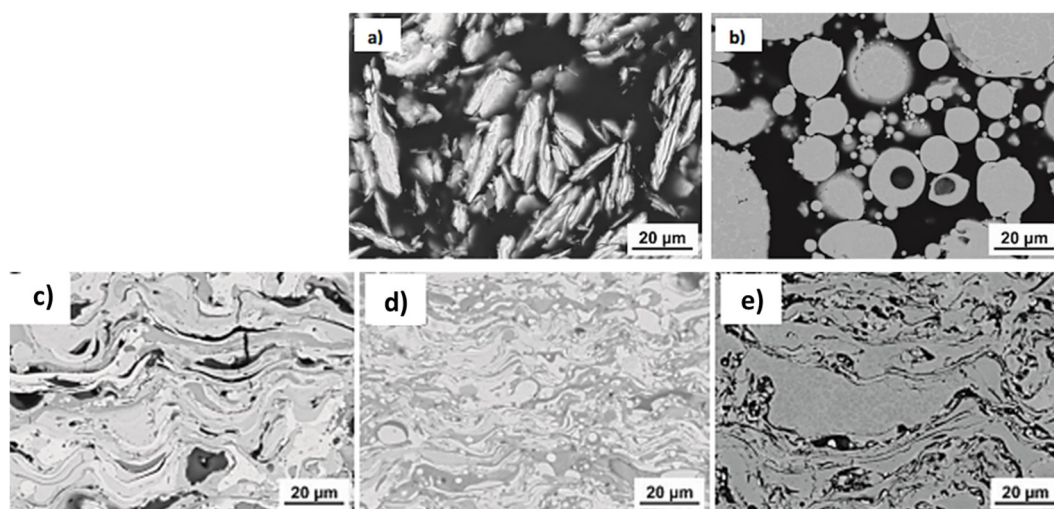


**Figure 3.** Backscattered scanning electron microscope images of (a) mechanically alloyed and (b) gas-atomized feedstocks of AlCoCrFeNiTi powders. Coating microstructure of the AlCoCrFeNiTi HEA coatings for (c) mechanically blended, (d) mechanically alloyed, and (e) gas atomized feedstock powders. The different microstructural features with respect to different feedstock powders are clearly visible in the figure, with the gas-atomized powder coatings showing homogeneity compared to the other two coatings [14].

Mechanical alloying and gas atomization are the most widely used synthesis routes for producing feedstocks for forming an alloy [12,16]. Due to the exceptional flowability and homogeneity in microstructural formations, the gas atomization method is a feasible method for synthesizing the HEA feedstocks. Mechanical alloying, on the other hand, has several advantages, which can enable the formation of nanocrystallinity, intermetallics, and even amorphous phases due to the diffusion of species into one another. When compared to the mechanically alloying routes, the impact of diffusion in the gas atomization is negligible because of the fragmentation of the molten metal into small droplets in a gas stream. However, the flowability of mechanical alloyed powders might be challenging due to their irregular morphologies and varying particle size distributions compared to that of a gas-atomized counterpart. Although different HEA compositions were scientifically explored by many researchers not only for thermal spraying but also for other deposition techniques, commercially available sources for the HEA feedstocks are limited. Table 1 lists the commercially available sources for HEA powders, which might be useful for thermal spray researchers who are eagerly looking forward to developing quality HEA coatings.

**Table 1.** The list of suppliers that provide high-entropy alloy feedstocks.

| Suppliers   | Type of Feedstocks   |
|---|----------------------|
| F.J. Broadmann & Co., LLC, Harvey, LA, USA                                | Mechanically alloyed |
| Vilory Advanced Materials Technology Ltd. Jiansgu, China                  | Gas atomized         |
| Eutectic powders, Edmonton, AB, Canada                                    | Gas atomized         |
| Stanford Advanced Materials, Lake Forest, CA, USA                         | Gas atomized         |
| Metal Powder Emergence Ltd., London, UK                                   | Gas atomized         |
| Kinaltek, Villawood, NSW, Australia                                       | Gas atomized         |
| Jiangsu Weilali New Material Technology Co., Ltd., Xuzhou, Jiangsu, China | Gas atomized         |
| Beijing Yanbang New Material Technology Co., Ltd. Xuzhou, Jiangsu, China  | Gas atomized         |
| ABM Nano INC, Missouri City, Texas, USA                                   | Mechanically alloyed |
| Sandvik Osprey LTD, Neath SA11 1NJ, UK                                    | Gas atomized         |

In contrast to these feedstocks synthesis routes, a new powder metallurgical technique has been introduced by Zhu et al. [17] to synthesize HEA powders rapidly by means of a plasma source provided by radio frequency inductively coupled plasma (RF-ICP). As shown in Figure 4, RF current, which is passed through a load coil wound around a dielectric tube (i.e., ICP torch), provides an intense electromagnetic (E.M.) field inside the torch leading to ionization of the working gas [17]. The mixed powders are placed on a water-cooled copper crucible that is able to tolerate the high temperatures of RF-ICP during the process (Figure 4).

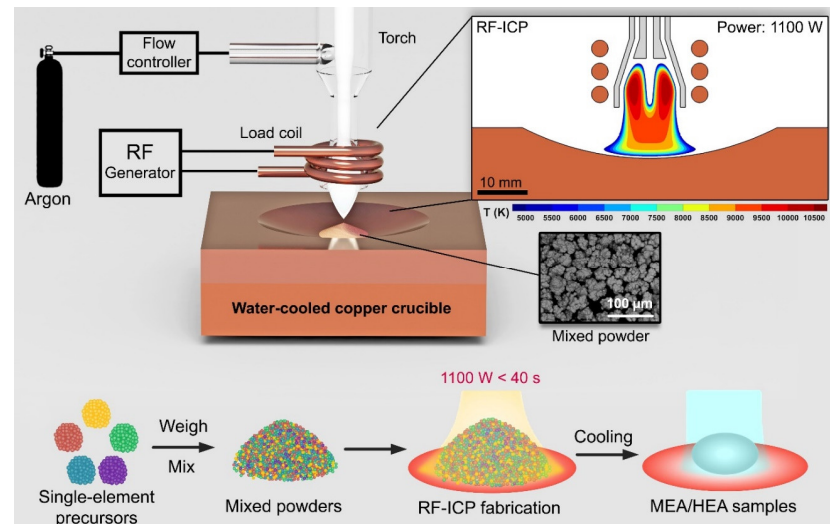


**Figure 4.** Setup of HEA synthesis with RF-ICP. Well-mixed powder bed is directly synthesized by RF-ICP under 1100 W with 5000–8000 K and becomes HEAs within 40 s [17].

The ignited RF-ICP rapidly heats the powder bed and builds up a high-temperature environment for HEA synthesis (Figure 5). Generally, the speed of material preparation in an alloy synthesis method is a critical factor. The process temperature provided by ICP can reach up to 5000–8000 K [17], which is significantly higher than 3000 K for arc-melting [18] and 4500 K for laser-melting [19]. Therefore, the efficiency of alloy synthesis by RF-ICP is higher. At the end of the process, the plasma is turned off while the argon gas keeps running to rapidly cool the sample while protecting it from the air [17]. As shown in Figure 5a, the total time is within 40 s for the fabrication of HEA, which is followed by fast cooling of the sample by argon for ~15 s. The pores seemingly disappeared after fast cooling (Figure 5a(I–V)). This method features a high fabrication temperature ensuring homogenous mixing, high heating, and cooling rate ( $\sim 10^5$  K/s), high fabrication speed preventing the material from volatile evaporation, reduction of the non-uniform distribution of microstructures caused by uneven diffusion due to high heating rate, eco-friendly heat source without the emission of harmful gases or secondary products to the environment, elimination of the unstable impurities, improved controllability of the process in comparison with the free burning arc due to the absence of arc instability, minimization of the contamination of the synthesized samples from electrode erosion due to electrodeless design of the RF-ICP, formation of a natural shroud gas around the sample by the plasma jet minimizing the entrainment of the surrounding air, and use of any kind of precursor in different physical forms or chemical compositions [17].

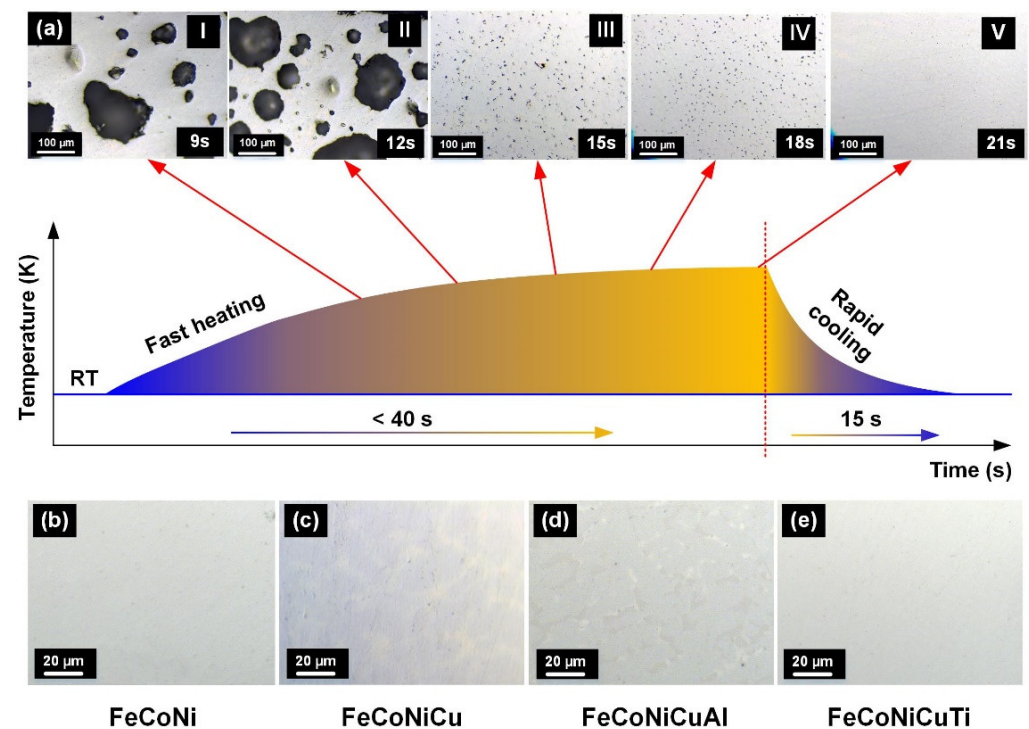


**Figure 5.** Rapid synthesis of alloys. (a) The temperature profile of CuNi alloy using the RF-ICP synthesis. The OM images demonstrate the evolution of the porosity of CuNi alloy during the HEA synthesis process. (b–e) OM images of synthesized FeCoNi MEA, FeCoNiCu MEA, FeCoNiCuAl HEA, and FeCoNiCuTi HEA [17].

### 3. Microstructure and Strengthening Mechanisms of HEA Coatings

#### 3.1. Microstructure

Thermal-sprayed deposits usually contain defects, such as porosities, un-melted or partially melted particles, and some level of oxides forming in the whole stages of the spray process [20–23]. Figure 6 illustrates the microstructural characteristics of AlCoCrFeNi HEA coatings, which are composed of three distinct phases with black, white, and gray regions. The high-entropy alloy coating displays a variety of splat types, including partially melted and unmelted regions. These microstructural artifacts are commonly observed in thermal spray coatings and can provide insights into the deposition process and resulting properties of the coatings. The occurrence of nano-sized precipitates within the splats might be a result of the non-equilibrium solidification process and the interaction among the constituent elements with different atomic sizes. As a result, the clusters and segregation of certain phases were formed, which may be the cause of nano-size precipitations. These precipitates can influence the mechanical property, such as the hardness and fracture toughness of the HEA coatings. All the HEA coatings developed through thermal spraying and their phase formations are summarized in Table 3.

It is worth mentioning that thermal spray coatings are comprised of defects such as voids and oxide contaminations. The density of these defects highly depends on the specific spray process used, the operating parameters chosen, and the feedstock sprayed. Several studies have indicated that investigating the relationships between defect formation and processing is vital for the improvement of as-sprayed coating properties [21,24–26]. The main defect of thermal-sprayed HEA coatings is oxidation. The existence of oxides breaks the chemical uniformity of coatings. Compared to the relatively soft HEA matrix, randomly distributed oxides are rigid. It has been reported that oxides play an important role in tribological applications [21,27–29]. In addition to increasing the hardness of HEA specimens, in certain conditions, oxides can act as self-lubricating materials. However, in

some cases, oxides with high porosity deteriorate the corrosion resistance, which can result in premature failure of the component [28,30,31].

Oxide formation takes place at different stages during the spray process [27]. The content of oxides highly relies on thermal spray processing. For atmospheric plasma spray (APS), where particle temperatures may reach up to 2500 K [32,33], the oxygen will react with fully molten or semi-molten powders before and after impact on a substrate. Oxide can be a major issue when HEAs have oxygen-sensitive constituents, such as aluminum (Al), titanium (Ti), chromium (Cr), and molybdenum (Mo) [16,34,35]. On the contrary, minimal oxidation was observed for the coatings deposited using cold spraying. The temperature used for this process is far below their melting points, which in turn results in lower oxidation [36–38]. More recently, a significant amount of effort has been put forward to reduce the content of oxides for APS [39–41]. By introducing a vacuum chamber in APS, the oxide inclusions will be efficiently reduced. However, apart from the limited workpieces, the cost of such installation is high. Instead, adding a coaxial shrouding gas is an efficient method to minimize oxidation.

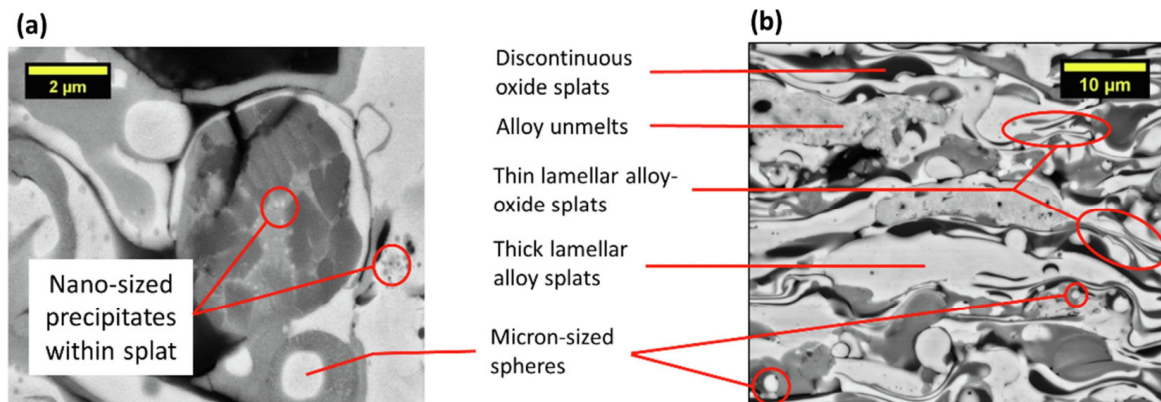


**Figure 6.** Backscattered scanning electron micrographs of atmospheric plasma spraying (APS) of AlCoCrFeNi HEA coatings. (a) shows a high-magnified image highlighting the nanoscale precipitates within the splats. (b) represents SEM images with different distinct regions (black, white, and gray phases) along with different splats (oxides, thick splats, thin splats, and partial and unmelted particles) [34].

HEA coatings developed via thermal spraying feature varying levels of porosity. The fraction of the porosity ranges from less than one percent to over ten percent. It is reported that the amount, size, and even the location of pores can strongly affect the mechanical properties (e.g., hardness, elastic modulus, wear behavior) and physical properties (e.g., thermal conductivity) of HEA coatings [21,23,42–48]. Table 3 lists porosity data as a function of thermal spray processes. It can be seen that the HEA coatings prepared via APS possess higher porosity compared to that of the HEA coatings developed via high-velocity oxygen fuel (HVOF) and cold spraying, respectively. In addition to that, varied particle distribution sizes of mechanically alloyed powder particles may induce microstructural defects with a high amount of porosity and cracks, which also depend on the exposed zones of powder particles in the plasma stream, as reported by Anupam et al. [34]. The particles traveling around the periphery of the plasma stream are not exposed to high temperatures completely, leading to partially melted regions or scattered fragments of oxides, which in turn, affects the homogeneity of the coatings and leads to undesirable properties (see Figure 7).

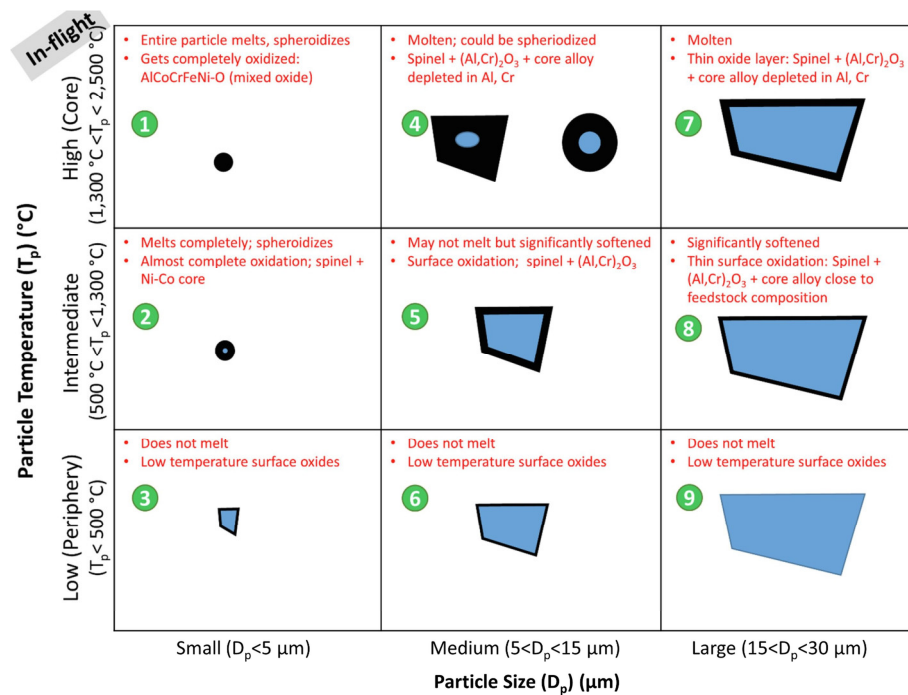


**Figure 7.** Schematic representation of how varying particle size ranges expose to the temperature and oxidizing atmosphere during in-flight [37].

A unique characteristic of thermal spray processes is the extremely high heating and cooling rates ( $>10^6$  K/s) [23]. Such rapid cooling rates result in fine-grain structures. Meanwhile, large numbers of solute atoms are also beneficial to limit grain growth in HEAs. Coatings with fine-grain structures often possess a good combination of strength and ductility. Another advantage of a high cooling rate is preventing elemental segregation. Therefore, as-sprayed HEA coatings may possess different phases' constitution compared with their as-cast counterparts [20,49–51]. For example, both  $\text{AlSiTiCrFeCoNiMo}_{0.5}$  and  $\text{AlSiTiCrFeNiMo}_{0.5}$  fabricated via thermal spray manifest a supersaturated BCC phase due to rapid solidification. For as-cast counterparts, they are dual-phase alloys (BCC + FCC) [49]. The phase compositions of HEAs are affected by the feedstock synthesis techniques and thermal spray methods. Mechanical alloying allows powders to mix in nanoscale with enhanced solid solubility, which favors the formation of solid solution phases before thermal processing [52]. Those post-alloyed powders melted or partially melted in APS, and HVOF will further undergo phase transformation. On the contrary, for cold spraying, due to relatively lower processing temperatures, materials will maintain their feedstock compositions. Taking Al-Co-Cr-Fe-Ni alloying system as an example, it was observed that the BCC phase dominates after mechanical alloying because aluminum acts as a BCC stabilizer [37]. This phase composition was retained in cold spray HEAs (see Table 3) [37]. For plasma-sprayed AlCoCrFeNi coatings, the FCC phase was observed as being the major phase [20]. However, this can be affected by the particle size, argon flow rate, and the spraying current. Coarse powders with an increment of argon flow rate favor the formation of the FCC phase [51].

The microstructure and phase constitutions can generally be adjusted by post-processing treatments. As-sprayed coatings, especially for those forming under high processing temperatures, have a high density of pores (see Table 3). The pores and microcracks are typically formed due to shrinkage of splats during rapid solidification, entrapped gases, and partial filling in the solidifying splats. Post-processing treatments have a strong influence on eliminating the pores. Yue et al. [53] proved that a dense surface with only very few isolated small pores can be found in the laser-remelted layer (shown in Figure 8a).

Besides, the growth of columnar dendrites was observed as the result of laser remelting (shown in Figure 8b).

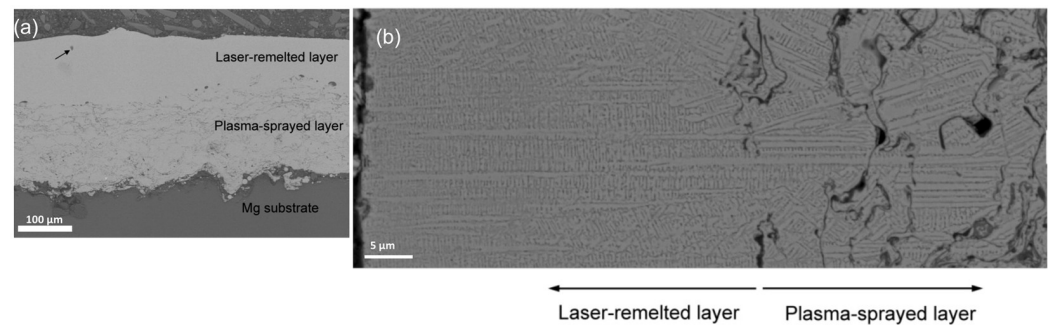


**Figure 8.** (a) A cross-sectional backscattered SEM image of AlCoCrCuFeNi coated on an Mg substrate showing the as-sprayed layer and a laser-remelted layer. (b) A high-resolution backscattered SEM image showing the epitaxial growth of columnar dendrites at the laser-remelted layer [53].

As mentioned above, rapid cooling rates allow HEA coatings to possess a precipitate-free microstructure. Annealing and/or laser remelting often promote the formation of precipitates [29,44,45,54]. The size and distribution of precipitates can be changed by tuning process parameters. Those precipitates as hard phases may increase the strength and hardness of HEAs and can be a good candidate in tribological applications. Wang et al. [54] applied a transmission electron microscope (TEM) on thermal-sprayed NiCo<sub>0.6</sub>Fe<sub>0.2</sub>CrSiAlTi<sub>0.2</sub> HEA coatings. After heat treatment, nanoprecipitates are randomly distributed in the matrix, which results in a higher hardness (935 HV) compared to its as-sprayed counterpart (450 HV). A high density of dislocations was observed after heating, and semi-coherent interfaces were formed, which is energetically favorable. In summary, the microstructures of HEA coatings can vary greatly depending on the chemical compositions and feedstocks employed. High-temperature deposition techniques, such as flame spraying and atmospheric plasma spraying (APS), can result in coatings with higher defects due to the oxidation and evaporation of certain elements, as well as high residual stresses caused by thermal mismatch, which can lead to cracking and delamination. Conversely, low-temperature techniques, such as cold spraying, can produce coatings with significantly fewer oxides (almost negligible) and high compressive stresses, enabling the formation of dense coatings with lower porosity levels.

### 3.2. Strengthening Mechanisms of HEA Coatings

This section primarily centers around the various strengthening mechanisms, such as solid solution strengthening, grain boundary strengthening, oxide-based strengthening, precipitation strengthening, and dispersion strengthening, which were achieved for different high-entropy alloy compositions that have been produced by using different thermal spray technologies. It is important to note that the mechanical properties, such as yield strength, fracture toughness, ultimate strength, and strain hardening, have not been measured extensively for HEA coatings. Thus, this section mainly focuses on the hardness property. Hardness is a crucial mechanical property for thermal-sprayed coatings in multiple applications as it can potentially offer benefits such as (a) wear resistance, which can resist microcutting and microploughing, making it suitable for abrasive environments, (b) corrosion resistance, which offers resistance against harsh chemical reactions, and (c) thermal resistance (or stability), where hard coatings can provide thermal shock resistance and withstand high temperatures, making them ideal for high-temperature applications.

#### 3.2.1. Solid Solution Strengthening

Based on the results from recent studies, the solid solution strengthening mechanism plays a major role in improving the strength of materials not only for bulk HEAs but also for the thermal-sprayed HEA coatings. Typically, HEAs are often stronger than traditional

engineering alloys because of their enhanced strengthening due to solid solutions. It has been reported that the solid solution strengthening for HEAs is mainly attributed to the pronounced lattice distortion associated with the mismatch parameter of atomic size differences of different elements [55]. The atomic radii of each constituent element studied for thermal-sprayed HEA coatings are illustrated in Table 2. As shown in Table 2, the elements with large atomic radii (i.e., Al, Ti, and Mo) induce strain energy in the lattice structure, causing severe lattice distortion, which is one of the core effects of high-entropy materials. The pronounced topological lattice distortion effect acts as a large barrier against the dislocations and their movements by effectively pinning the dislocations, yielding solid solution strengthening/hardening. A study by Wang et al. [56] explored the deposition of gas-atomized AlCoCrFeNi feedstock on AISI 1045 steel by means of APS. The hardness was around 4.5 GPa (468 HV), which is likely due to the solid solution strengthening caused by the disordered BCC (A2) and ordered BCC (B2) phase formations. The different phase formations in accordance to the HEA compositions and thermal spraying are illustrated in Table 3. It has been argued that the occurrence of ordered B2 phases is more prominent when the lattice distortion effect is too large [55]. The movement of dislocations is inhibited by the hard B2 phases causing resistance to plastic deformation, which further yields improved strength for the HEA coatings. The effect of annealing temperature on hardness has also been investigated for the AlCoCrFeNi coating, and the results showed an increase in hardness with lower annealing temperature and a gradual decrease as the function of annealing temperature (from ~600 to 900 °C). The higher hardness obtained after annealing at 600 °C (5.64 GPa) was approximately 1.2 times than that of the as-sprayed HEA coatings at room temperature. The authors claimed that the area fraction of B2 phases (i.e., possible increase in the solid solution strengthening effect) increased at 600 °C, thus significantly contributing to enhanced hardness. Nonetheless, it is anticipated that the presence of B2 phases declines the toughness/ductility of the coatings that have not been reported to date.

**Table 2.** Shows the atomic size radius of the constituent elements used for high-entropy alloy coatings.

| Elements                | Al    | Co    | Cr    | Fe    | Ni    | Ti    | Si    | Mn    | Nb    | Mo    |
|-------------------------|-------|-------|-------|-------|-------|-------|-------|-------|-------|-------|
| Atomic size radius (nm) | 0.143 | 0.125 | 0.128 | 0.127 | 0.125 | 0.146 | 0.111 | 0.126 | 0.246 | 0.139 |

Mu et al. [57] explored AlCoCrFeNi equimolar compositions deposited by means of atmospheric plasma spraying. The authors showed that the average hardness increased as a function of spraying power, with the highest observed around 5.97 GPa while using a voltage and current of 55.4 V and 550 A, respectively. Cheng et al. [51] investigated similar AlCoCrFeNi HEA composition deposited using APS with varying gas atomized feedstocks (10–60 µm and 60–90 µm). The hardness was higher (4.18 GPa) for the coatings deposited with coarser feedstock (60–90 µm) and a high spraying current of 650 A. This was mainly attributed to the solid solution strengthening associated with BCC phases compared to finer feedstock (which has major FCC peaks). It should be noted that the absence of oxides was reported compared to the other literature on APS-based HEA coatings. However, it can be inferred that the solid solution strengthening due to the presence of high aluminum content (20 at%) is the major responsible factor for a high hardness.

The microhardness and wear properties of mechanical-alloyed AlCoCrFeNiTi HEA coatings were first investigated by Tian et al. [16]. The authors used the APS technology to fabricate the coatings on stainless steel 316 substrates. The result showed that the average hardness value was around 6.3 GPa (642 HV<sub>0.2</sub>), which was higher compared to the AlCoCrFeNi HEAs fabricated by means of atmospheric plasma spraying. The hardness of 3.8 GPa was also obtained at the coating/substrate interfaces, signifying adequate adhesion. The interface hardness is significant because it can influence the adhesion strength and durability of the coatings. A higher interface hardness generally indicates better adhesion strength, as the coating can better resist separation from the substrate under

mechanical or thermal stress. The low porosity, severely distorted lattice structure (solid solution strengthening) due to large atomic radii of aluminum and titanium, as well as the hard oxides are the determinative factors that contribute to the improved hardness of AlCoCrFeNiTi coatings.

Generally, silicon can also increase the strength of the materials through solid solution strengthening due to its small atomic size compared to other constituent elements. In terms of HEAs, the addition of silicon favors to phase transitions (ordered and/or disordered BCC structures) and mechanical properties due to its high negative enthalpy of mixing with other constituent elements and lattice distortion effect. To date, the influence of silicon content on the mechanical properties has been limitedly examined. Tian et al. [58] fabricated the equimolar AlCoCrFeNiSi HEA coatings using the APS technique on stainless steel 316L. The average hardness was found to be approximately 6 GPa (612 HV<sub>0.2</sub>), which is due to the solid solution strengthening associated with the presence of B2 and disordered BCC phases.

### 3.2.2. Grain Boundary Strengthening

Grain boundary strengthening or fine grain strengthening are often observed in thermal-sprayed HEA coatings, particularly in cold spraying, which can significantly contribute to the enhancement in the hardness/strength. For grain boundary strengthening, the strength/hardness primarily depends on the pinning of dislocations around the fine grains contributing to the Hall–Petch effect. This phenomenon has been observed in cold-sprayed HEA coatings, as reported by Nair et al. [59] and Rojas et al. [60]. The high-velocity impact offered in thermal spraying techniques (cold spraying, HVOF, and HVAF) improves the strengthening by inhibiting grain growth due to dynamic recrystallization and high dislocation density [60]. A comparative study of AlCoCrFeNi HEA coatings developed using HVOF and HVAF thermal spray technologies was reported by Lobel et al. [61]. The microhardness exhibited higher values (6.6 GPa) for HVAF-fabricated HEA coatings compared to that of HVOF-based HEA coatings (5.8 GPa). The authors concluded that the low porosity levels and influence of grain boundary strengthening (fine grain size) due to high-velocity impact could be the possible reasons for improved hardness for the HVAF coatings. Furthermore, the absence of oxides and low porosities also resulted in a low standard deviation of hardness for the HEA coatings developed using HVAF techniques.

In a different study reported by Wei et al. [62], for similar composition HEA fabricated by means of HVOF, the average microhardness obtained was around 5.4 GPa (552 HV<sub>0.3</sub>), which was attributed to the presence of FCC and BCC phases. The authors also performed nanoindentation testing to determine the nanohardness and elastic modulus of each phase (FCC and BCC phases). Higher nanohardness (i.e., 9.5 GPa) and lower elastic modulus (i.e., 208 GPa) were obtained for the BCC phases when compared to that of the FCC (i.e.,  $H = 5.9$  GPa and  $E = 250$  GPa), highlighting solid solution strengthening. The work of elastic deformation was high in BCC phases, indicating the capability of large elastic recovery after deformation compared to FCC phases. The study concluded that the combined interaction of solid solution strengthening and grain boundary strengthening are the contributing factors to the improvement in the hardness of the HEA coatings. Similarly, Liao et al. [63] investigated the hardness of the Cantor (CoCrFeMnNi) HEA deposited by means of detonation spraying on stainless steel 316L substrates. The average hardness obtained in this study was around 4.6 GPa, which outperforms the alloys fabricated using casting (1.6 GPa) [64] and spark plasma sintering (4 GPa), respectively [65]. Despite the presence of FCC phases in the CoCrFeMnNi coatings, the grain boundary strengthening associated with fine grains and oxide formations augmented the high hardness.

While thermally sprayed HEA coatings exhibited outstanding microstructural features and mechanical properties, as shown by several studies in the literature, there is limited work specifically focusing on HEAs fabricated via cold spray techniques. The trend in cold-spray HEA coatings is increasing among researchers due to their feasibility in producing high-strength coatings [66,67]. The high velocity (typically between 500 m/s

and 1200 m/s) during the deposition process results in severe plastic deformation, which further contributes to improved strength due to fine grain size and work hardening. Anupam et al. [37] reported the first AlCoCrFeNi HEA fabricated by means of cold spraying. The mechanically alloyed powder feedstocks were used to deposit the coating on nickel superalloy substrates. The major BCC phase obtained for the HEA resulted in an average coating hardness of 3.8 GPa. The high hardness could possibly be explained by the fine grain structure, which occurred due to severe plastic deformation. However, the obtained hardness value for the cold-sprayed AlCoCrFeNi HEA coatings was lower compared to HVOF- and APS-deposited HEA coatings [51,61], which is due to the absence of oxides lamellae in the cold spray HEA coatings. The Cantor alloy (CoCrFeMnNi) was investigated by Yin et al. [38] by using a high-pressure cold spray system to deposit atomized CoCrFeMnNi feedstock on aluminum 6082 alloy substrates. The overall microhardness showed to be around 3.2 GPa, which was three times the hardness of powder particles. The improvement in the hardness was attributed to the significant grain refinement (fine grain strengthening) and increased dislocation density after cold spraying.

### 3.2.3. Oxide-Based Strengthening

The evolution of oxides and their impact on the mechanical properties of thermal spray coatings has been previously reported on several occasions. The occurrence of oxides during oxidation in-flight for high-temperature deposition techniques is a common artifact. Nevertheless, the occurrence of these oxides plays a dominant role in changing the behavior of the coatings in terms of hardness and wear performance. Meghwal et al. [68] conducted nanoindentation studies on similar compositions fabricated using APS. The oxide phases were dominant in the case of APS HEA coatings compared to the HVOF HEA coatings. The Al-rich and oxide-rich phases were found to have the highest nanohardness of 15 GPa, followed by AlCrFe oxides and Al-depleted HEA regions with 13 GPa and 5 GPa, respectively. The  $H/E_r$  (hardness to reduced elastic modulus) ratio was reported to be lower for the Al-depleted HEA phase, indicating the ability to resist plastic deformation. Although the Al-rich oxide phases exhibited high hardness, the Weibull plot assessment signifies the Al-rich oxides phases with the largest variations, which explained the inhomogeneity of property distribution. These oxides improved the overall microhardness of the AlCoCrFeNi HEA coatings, which was around 4.13 GPa. It should be noted that the measured microhardness using Vicker's diagonal impression is a delicate balance between the different microstructural artifacts, such as microstructural defects (pores and cracks) and multiple phases of the coatings, which differ from the nanohardness of each phase. Liang et al. [69] investigated APS-based non-equimolar  $Al_{0.5}CoCrFeNi_2$  high-entropy alloy coatings using gas-atomized powders. The average hardness reported was around 2.7 GPa, which was lower than that of the same coatings developed using magnetic sputtering (5.5 GPa). The reason might be the homogenous microstructure with low defects and voids, resulting in two times high hardness for the sputtered HEA coatings.

More recently, Nair et al. [59] investigated novel AlCoCrFeMo HEA using cold spraying and flame spraying technologies to understand their effects on the microstructural formation and hardness properties. The average hardness showed approximately 40% improvement for the flame-sprayed HEA coatings owing to the formation of a high fraction of spinel ( $AB_2O_4$ ) oxides (25 wt%) compared to cold-sprayed HEA coatings, despite having similar BCC phases. A comparative study using APS and HVOF was investigated by Li et al. [70] using non-equimolar  $FeCoCrNiMo_{0.2}$  HEA as feedstock. The average hardness reported for APS and HVOF coatings was around 3.4 GPa and 3.8 GPa, respectively. The reported values also outperform the  $FeCoCrNiMo_{0.3}$  HEA fabricated via arc melting (2 GPa) investigated by Shun et al. [71]. Although the coatings and arc-melted HEAs exhibited FCC phases, the improvement in the hardness for the HEA coatings was mainly attributed to the occurrence of oxide contaminations compared to that of arc-melted HEAs.

### 3.2.4. Dispersion Strengthening

The particulate-reinforced high-entropy alloy coatings developed by means of thermal spraying techniques have been reported in the literature [72–74]. The hard particle reinforcement enhances the mechanical properties such as hardness and toughness due to the different possible mechanisms, namely, (i) dispersion strengthening—associated with micro size particles, (ii) a misfit in coefficient of thermal expansion—resulting in the occurrence of geometrically necessary dislocations, (iii) load transfer effect—transferring loads from the matrix to the particles and (iv) Orowan strengthening mechanism associated with nano-size particles [75]. It has been reported that the addition of micron-sized particles induces high dislocation densities and twinning around the reinforced particle regions, which contributes to improvement in the hardness/strength [76]. Many studies have been reported on the effect of dispersion strengthening through particle-reinforced HEA coatings. Wei et al. [72] investigated the effect of hard WC-10Co reinforcement of AlCoCrFeNi HEA coatings by mixing using a mechanical mixer prior to deposition. The HVOF system was used to spray these in different proportions (i.e., from 0 to 50 wt.% of WC-10Co) on 06Cr13Ni5Mo martensitic stainless steel. The average hardness showed a linear function with the reinforced particles, with the highest value obtained for equi-proportional HEA composite coatings (7.3 GPa), which was around 1.5 times higher than non-reinforced counterparts. The solid solution strengthening associated with high atomic radii elements (aluminum), as well as the dispersion strengthening mechanisms (due to hard WC-Co particles) further results in improved hardness for the HEA coatings. Moreover, the addition of reinforcement enhanced the plastic deformation resistance of the coatings obtained from nanoindentation results. The nanohardness and elastic modulus of BCC phases were around 11.52 GPa and 232 GPa, respectively, for the equi-proportional HEA composite coatings, which was higher than the values reported previously [62]. This can be explained based on the bonding force enhancement of the lamellae after reinforcement additions, which further resulted in an enhancement in the average hardness. The improved interface bonding could effectively result in load transfer from the matrix to the particulate, hence contributing to improving hardness.

In the work reported by Tian et al. [15], the atomized Ni60 alloy was added as a reinforcement to AlCoCrFeNiTi and fabricated using the APS technique. An increase in the average hardness from 6.3 GPa to 6.6 GPa was found after reinforcement addition, which is attributed to dispersion strengthening and solution hardening. The coating/substrate interface hardness was also enhanced noticeably after the reinforcement additions compared to non-reinforced counterparts. Zhu et al. [74] investigated MnCoCrFeNi composite HEA by adding Al<sub>2</sub>O<sub>3</sub>-13 wt.% TiO<sub>2</sub> as a reinforcement and fabricated via APS. The powders were blended with a 3D motion mixer with a frequency of 50 Hz for 4 h before spraying. The average hardness was 1.29 times higher for the HEA coatings after reinforcement, signifying the dispersion strengthening. The H/E ratio was also enhanced, indicating increased resistance to plastic deformation and elastic recovery for the Al<sub>2</sub>O<sub>3</sub>-13 wt.% TiO<sub>2</sub>-reinforced HEA composite coatings.

Nano oxides reinforced FeCoCrNiMo HEA using APS were investigated by Mu et al. [57]. The authors concluded that there was dispersion strengthening (possibly Orowan strengthening) due to the addition of nano-oxides as well as solid solution strengthening due to the high atomic size of molybdenum. These contributed to the high microhardness of 3.1 GPa despite the FCC structure. The obtained average hardness was almost similar to the result obtained using APS FeCoCrNiMo0.2 HEA coatings [70] and was higher than arc-melted HEAs [71].

### 3.2.5. Precipitation Strengthening

The effect of precipitation strengthening on the mechanical properties of thermal-sprayed HEA coatings has been reported in the literature. Fine particles that precipitate create large strain fields, which act as barriers to the movement of dislocations and improve the hardness through Orowan strengthening [75]. A very recent study by Rojas

et al. [60], reported the formation of a nano-sized fine precipitate (226 nm) for cold-sprayed  $\text{CoCrFe}_{0.75}\text{NiMo}_{0.3}\text{Nb}_{0.125}$  HEA coatings. The authors concluded that the fine precipitates, coupled with lattice distortion induced by molybdenum and niobium (solid solution strengthening), and fine grains (grain boundary strengthening associated with cold spraying) pinned the dislocations resulting in high compressive yield strength of 1745 MPa. Jin et al. [77] investigated the effect of silicon in different molar fractions ( $x = 0.5$  to 2) on  $\text{Al}_{0.5}\text{CoCrFeNiSi}_x$  HEA fabricated by means of APS on Q235 steel substrates. As mentioned previously, the addition of Si favors the solid solution strengthening the HEA due to their small atomic size compared to those of constituent elements present in the composition. The developed coatings were post-processed using laser re-melting. The hardness showed linearity with the molar fractions, wherein the maximum hardness was observed for  $\text{Al}_{0.5}\text{CoCrFeNiSi}_2$  coatings (10.7 GPa), and the lowest hardness was found for the coatings with low silicon content (4.9 GPa). The area fractions of BCC phases increased (increase in solid solution strengthening effect) by suppressing the FCC phases after laser-remelting, which contributed to the highest hardness for the coatings. However, due to the high silicon, chromium, and silicon content (which has a high negative enthalpy of mixing), it tends to decompose from the matrix and form  $\text{Cr}_3\text{Si}$  precipitates, which also act as a precipitation strengthening mechanism and along with solid solution strengthening due to lattice distortion, it further resulted in high hardness.

Li et al. [69] reported non-equimolar  $\text{Al}_{0.2}\text{CrCo}_{1.5}\text{FeNi}_{1.5}\text{Ti}$  HEA by adding silver as a reinforcement to fabricate coatings using APS. The HEA and reinforced particles were mechanically blended and deposited on carbon steel substrates. The coated specimens were then heat-treated to 750 °C. The average hardness showed to be around 6 GPa for as-sprayed HEA coatings, which further increased up to 1.2 times after heat treatment. The oxidation and precipitation hardening (Ni-Ti and Co-Ti phases) are the contributing factors for improved hardness after heat treatment. Moreover, the addition of silver (2 wt%) to the HEA coating act as dispersion strengthening that reduced the overall wear rate and friction coefficient at high temperatures. A recent study by Yurkova et al. [47] explored the MA  $\text{AlCoCrFeNiTi}$  HEAs deposited using high-pressure cold spraying on steel substrates. The study reported that the average hardness value is around 10 GPa, which outperforms the  $\text{AlCoCrFeNiTi}$  coatings fabricated by means of APS and HVOF techniques [14,78]. The presence of intermetallic phases, such as B2 (AlNi rich) and CrFe rich precipitate phases along with TiC formations, contributed to high hardness. The titanium residue that did not bond with the BCC phase during mechanical alloying was reacted with carbon (which is present in the carbon-containing gas, i.e., acetylene) during spraying to form TiC, thus contributing to higher hardness [78]. In addition, the high-velocity impact of feedstock powder particles on the substrate resulted in significant plastic deformation through strain hardening and undergoing dynamic recrystallization, which influences further hardness enhancement.

Another study was performed by Chen et al. [79], where the authors reduced the Al content to  $\text{Al}_{0.6}\text{CoCrFeNiTi}$  HEA. The average hardness value obtained for the HVOF-sprayed HEA coating was around 7.7 GPa (789  $\text{HV}_{0.1}$ ). The hardness increased up to 9.2 GPa when treated at a temperature of 800 °C for 1 h. The improved hardness was probably related to the precipitation hardening after heat treatment. The CrFe-rich  $\sigma$  phases were precipitated from the BCC phases at high temperatures (>300 °C), resulting in a high hardness. Furthermore, the fracture toughness was investigated using the Vickers indentation method for the first time in thermal spray coatings. Higher fracture toughness was obtained at room temperature (8.4  $\text{MPa}\cdot\sqrt{\text{m}}$ ). However, the fracture toughness showed to be decreasing after heat treatment (5  $\text{MPa}\cdot\sqrt{\text{m}}$ ). These trends can possibly be explained by the brittle nature of CrFe-rich  $\sigma$  phase precipitations. At high temperatures, the CrFe with high negative enthalpy of mixing tends to decompose from the BCC phases forming  $\sigma$  phase precipitates. The presence of  $\sigma$  phases also increases the work hardening ability due to the formation of deformation twinning and, hence, improves the hardness and lowers fracture toughness. The detailed mechanism needs to be further investigated to provide a

correlation between phase formations and mechanical properties. The various high-entropy alloy coatings developed through thermal spraying techniques that have been evaluated in terms of their strength/hardness are summarized in Figure 9. As shown in Figure 9, the precipitation strengthening mechanism, together with solid solution strengthening, contributes to higher microhardness when compared to the other strengthening mechanisms of the HEA coatings, irrespective of the chemical compositions and deposition technologies.

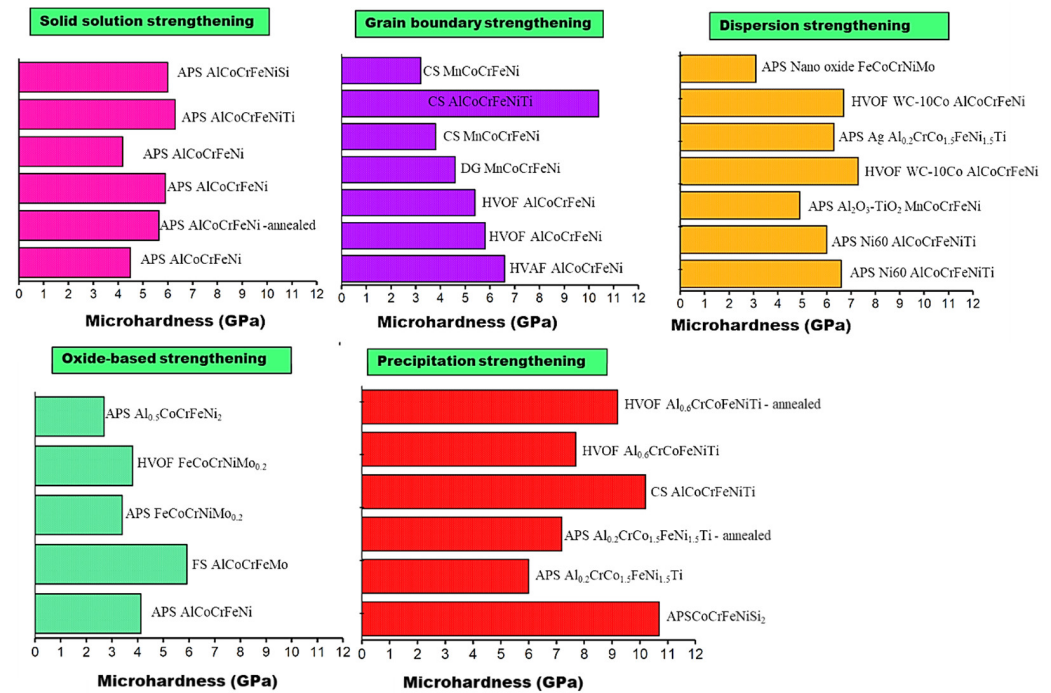


**Figure 9.** Comparative assessment of different strengthening mechanisms for thermal-sprayed HEA coatings. The precipitation strengthening seems to have a higher influence on the microhardness compared to all other strengthening mechanisms [16,38,47,51,56–80].

### 3.3. Quantitative Mechanical Performance and Property Assessment for Extreme Industrial Applications

The influence of microstructure and mechanical properties incline to form in thermal spray HEA coatings are important to understand the failure mechanisms due to loading conditions. The results from the previous studies of HEA coatings are investigated mainly on micro-hardness. Although hardness is a dominant property, the reliability of the coatings under different loading conditions is also influenced by various mechanical properties such as yield strength, ultimate strength, ductility, toughness, strain hardening, and elastic modulus. Recently, Munday et al. [80] studied the correlation between different mechanical properties and microstructural features (porosity, particle-particle mean free path, and average particle size) on cold-sprayed WC-Ni composite coatings. The features of microstructural defects that influence mechanical properties have been investigated systematically. It was reported that a high variation in tensile strength was found due to variations in WC content and related porosity. Such a study may open the door to exploring the fundamental understanding of HEA coatings. The high spatial variability is challenging and difficult to address experimentally and can be validated and predicted by mechanism-based numerical models.

The strength and toughness are the key properties that determine resistance to damage due to loading. For instance, the aircraft and marine components during operations suffer from erosion damage due to the impact of high-velocity solid particles, which results in a decline in the efficiency of the components and premature failure. Furthermore, the decline in the wear performance may drastically lead to fatigue failure due to cracking [81]. The fatigue crack initiation phenomenon is related to the residual stress, and the coatings with

an excellent balance of strength and toughness can provide high resilience to fatigue, wear, and erosion damages [82,83]. However, the systematic investigations that relate to the HEA coatings and their fatigue failure mechanisms are lacking. It has been reported that the material's capability to absorb strain energy can provide high damage tolerance to fatigue failure. Furthermore, it is well-known that the coatings with excellent toughness and ductility can provide resistance to erosion damage for an angle of impact greater than  $60^\circ$ , whereas hardness and strength are the dominant parameters at low angles [83,84]. HEAs are reported to have a concurrent combination of strength and toughness, which can provide resistance to micro-cutting, micro ploughing, micro-indent, and micro-cracks [85–87]. Since the state-of-the-art of the field of HEAs is established among thermal spray researchers, such studies have not been explicitly explored to date.

Figure 10 represents classifications of parameters that should be quantified for extreme engineering environments. Correlating the materials-related features of HEA coatings, including different mechanical properties (yield strength, ductility, toughness, ultimate strength, fracture strength, elastic modulus, work hardenability, fracture resistance), microstructures (porosities, cracks, inter-splat bonding, adhesion, and cohesion), and phase formations (oxides, FCC, BCC, and other phases) with extrinsic factors of wear damage, such as shape and size of abrasion particles, particle distribution, hardness of the abrasive particles, density, impact velocity, impact angles, and temperature, may help in understanding the effect of microstructure, mechanical properties, and loading conditions (see Figure 10). However, such process parameter evaluations are challenging through experimental investigations and not fully understood. The mechanism through physical-based modeling is a viable approach to predict the damage resistance of thermal-sprayed HEA coatings.

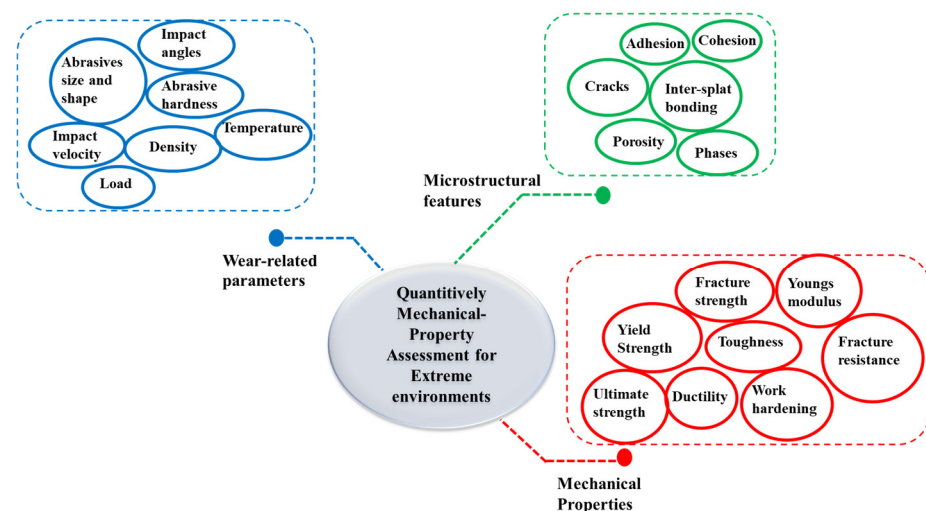


**Figure 10.** Schematic illustrating the classifications of material properties for quantifying the mechanical performance for extreme environmental applications.

Other salient properties that influence the functionality of a coating are the substrate-coating adhesion and cohesion or bonding between splats. The adhesion and cohesion strengths can appreciably affect the coating's performance in various loading conditions. These studies are not emphasized to date for thermal spray HEA coatings. Thus, the fundamental understanding of the adhesion and strengths and their mechanisms on wear loading need to be explored for HEAs as structural applications. The bond strength can be investigated by various testing, which includes peel adhesion [88,89], laser shock adhesion test [90,91], and three-point bend test [92]. However, the application of these methods on thermal-sprayed HEA coatings has not been explored, and further research is required.

## 4. Performance Assessment of HEA Coatings

### 4.1. Wear Behaviour

High-entropy alloys by means of thermal spraying that have been studied so far in terms of friction and wear are shown in Figure 11. The majority of HEA compositions studied contain CoCrFeNi elements, with the addition of Al, Ti, Mn, and Mo investigated under different sliding conditions. While thermal spraying was not used to investigate different HEA chemical compositions, researchers extensively studied the CoCrFeMnNi (Cantor alloy) HEA coating. This equimolar HEA possesses a single-phase solid solution structure with excellent fracture toughness. Additionally, different derivatives of the Cantor alloy, with aluminum and titanium additions (replacing Mn) fabricated by means of thermal spraying, were also extensively investigated and reported. The addition of aluminum to CoCrFeNi HEA systems improves the coatings' strength by stabilizing BCC, with higher Al fractions (or equimolar fraction with other constituent elements) leading to stronger HEAs, while lower Al fractions (<20 at%) promote the FCC structure. The addition of Ti to CoCrFeNi enables lower density and high hardness while also providing self-lubricating behavior. Replacing Mo with Ni also results in excellent strength for HEA materials due to the stabilization of BCC and excellent lubrication, which helps lower friction and wear. Since the HEA coatings could provide high-temperature wear performance due to their peculiar microstructural features, many studies were also devoted to performing the wear studies at elevated temperatures. However, it is clear from Figure 11 that the HVOF and APS are the mainly employed deposition techniques to fabricate different chemical compositions of HEAs to investigate friction and wear performances; thus, there is a significant gap in understanding how other spray coating technologies influence the wear performance of HEA coatings.

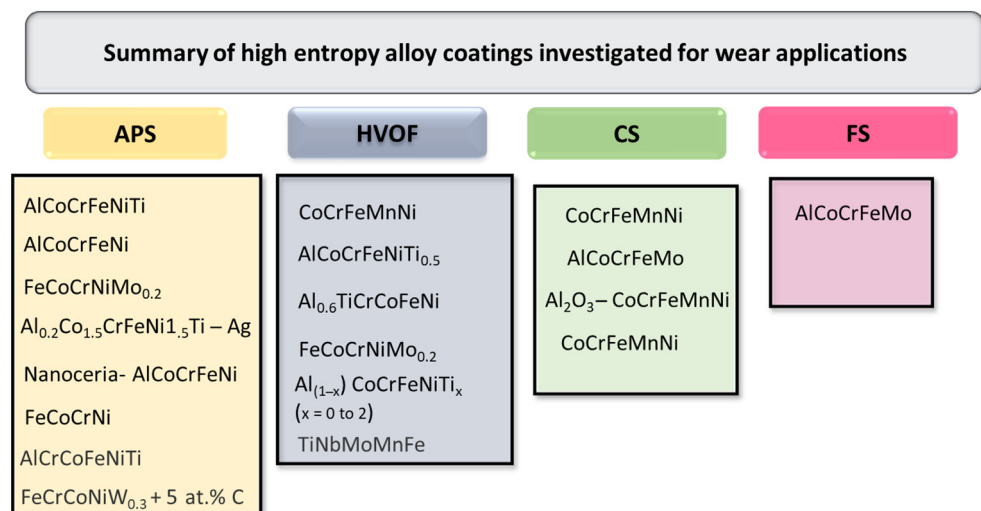


**Figure 11.** Summary of different thermal-sprayed HEA coatings investigated for wear behavior.

Friction and wear were systematically investigated for different HEA coatings by varying one or more testing parameters such as velocities, loads, temperatures, and time in order to understand the impact of these parameters on wear mechanisms and tribofilm formations. It should also be noted that different counter balls such as alumina, Si<sub>3</sub>Ni<sub>4</sub>, and WC-Co were also considered by the authors to slide against the HEA coatings, depending on their conditions and equipment feasibility. However, the significance of using different counter balls against HEA coatings was not explicitly explained in the literature. Hence, this section provides some of the key aspects of thermal spray HEA coatings on friction and wear behavior.

The wear behavior of AlCoCrFeNiTi<sub>0.5</sub> developed by means of HVOF was studied as a function of temperature (room temperature to 900 °C) using an Al<sub>2</sub>O<sub>3</sub> counterface and

a 26 N normal load [93]. A strong dependence of temperature on the wear behavior was observed, which indicates that the wear resistance decreased as a function of temperature (from room temperature to 500 °C) due to thermal softening. However, an increase in the wear resistance was found as the temperature increased up to 900 °C. Figure 12 revealed the presence of deep grooves with oxide formations (white regions) at the lowest temperature. However, an oxide film or glazed layers appeared to be compact on the wear tracks at elevated temperatures, acting as a protective shield against plastic deformation [93]. The glazed layers formed are comprised of spinel oxides, causing a reduction in the coefficient of friction and wear rates.

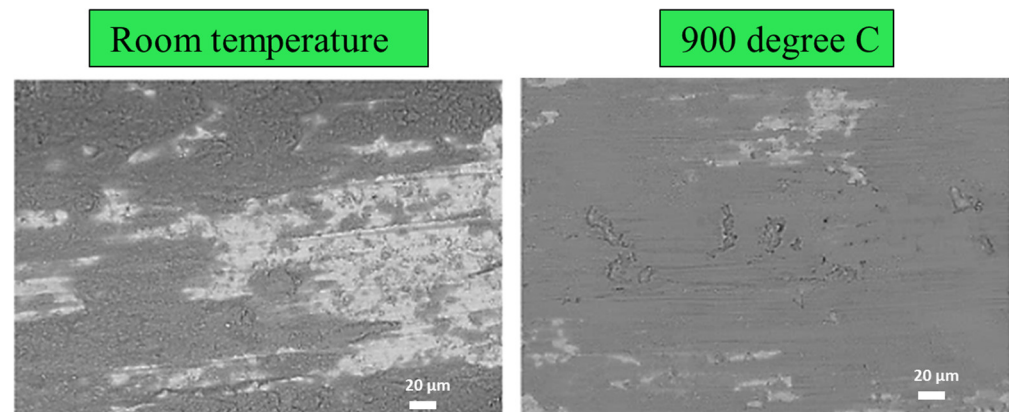


**Figure 12.** Wear morphologies of AlCoCrFeNiTi HEA coatings tested at room temperature and elevated temperature (secondary electron mode). The presence of contrast oxide regions was more profound when tested at room temperature compared to that at elevated temperature [14].

Chen et al. [79] investigated the wear performances of HVOF-based  $\text{Al}_{0.6}\text{TiCrCoFeNi}$  HEA coatings using pin-on-disc testing against an  $\text{Al}_2\text{O}_3$  counter body. The authors noticed a change in the wear behavior as a function of temperature, wherein abrasive wear was the dominant wear mechanism, together with fatigue failure at an increased temperature [79]. A compact glazed layer was also identified on the wear tracks at the highest temperature (500 °C), yielding to a reduction in the coefficient of friction. The evolution of these compact glazed layers protects the surface from further damage due to sliding, and thereby lower wear rates were achieved [79].

A more recent study by Patel et al. [94] investigated the wear behavior of as-sprayed and heat-treated CoCrFeMnNi HEA coatings using  $\text{Al}_2\text{O}_3$  as a counter surface tested at 5 N normal load. The study was carried out on rough and polished surfaces, aiming to understand the influence of surface roughness on tribological interfaces. The as-sprayed polished surfaces showed approximately five times lower wear rates compared to those of rough surfaces of the HEA coatings, indicating that rough surfaces are not a favorable method for wear applications. However, no variations in wear rates were achieved after heat-treating the HEA coatings. The difference in wear rates could possibly be explained by the formation of oxide or glazed layers, which were similar in the case of as-sprayed and heat-treated HEA coatings. The authors concluded that the occurrence of tribolayers (typically mixed oxide layers) acts as the third-body, which reduced the adhesion between the two bodies and thereby increased the wear resistance for both coatings [94].

Recently Supekar et al. [95] studied the sliding wear characteristic of a new composition of AlCoCrFeMo HEA fabricated by low-pressure cold spraying and flame spraying techniques. In this study, the authors also used  $\text{Al}_2\text{O}_3$  as a counter ball and performed at a constant velocity by varying loads (i.e., 5 N and 10 N). Interestingly, the frictional coefficient was found to be lower for cold-sprayed HEA coatings despite the lower hardness compared to the flame-sprayed counterparts. The formation of loose debris (predominantly oxides due to frictional heating) between the tribo pairs acting as a roller bearing during sliding was the governing factor for the lower frictional coefficient for cold-sprayed HEA coatings.

Nevertheless, the wear rates were lower for the flame-sprayed HEA coatings, which is due to the higher hardness resulting from spinel oxide inclusions and BCC phases. However, the cold-sprayed HEA coatings underwent third-body abrasion, with the removal of oxide layers causing higher wear rates during sliding. Figure 13 shows the counterface images after sliding against the HEA coatings at both the surface conditions. As shown in Figure 13, the material transfer had taken place for all the coatings. The counter spheres against flat cold-sprayed HEA coatings showed greater material transfer than those of flame-sprayed HEA coatings, with very little evidence of transfer layers. This also correlated well with the cold-sprayed HEA coatings, with increased wear rates.

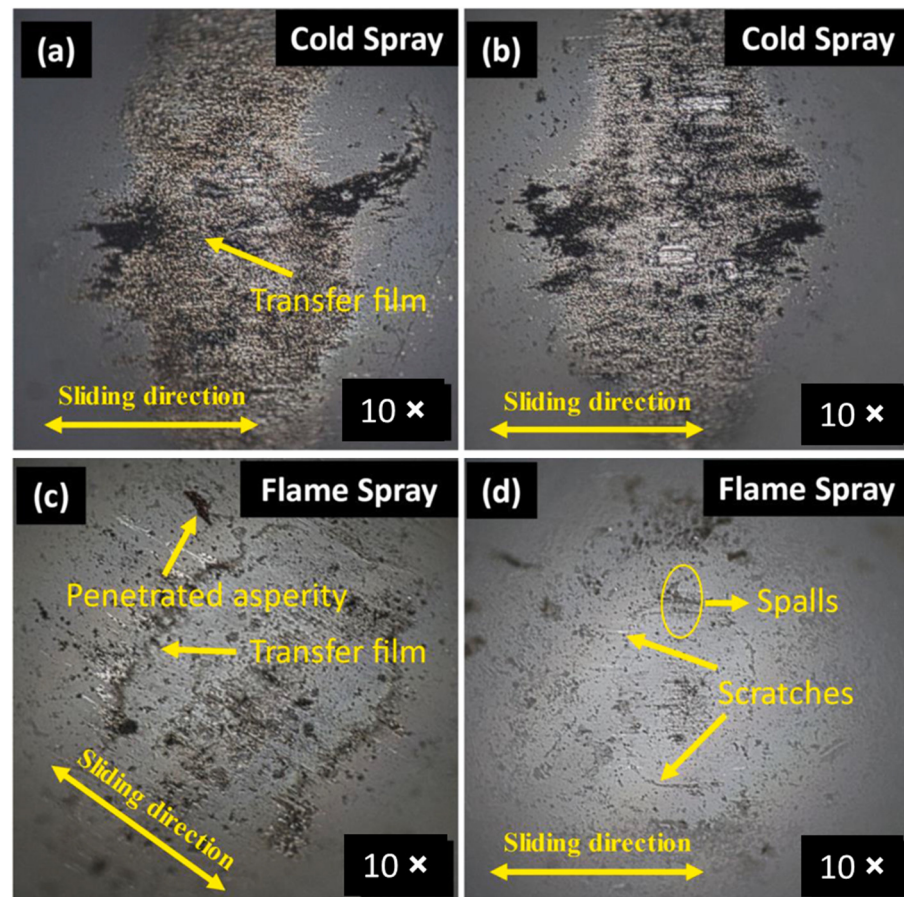


**Figure 13.** Optical microscopy images of alumina counter balls after sliding at 5 N load for (a) unpolished, (b) polished cold-sprayed HEA coatings, (c) unpolished and (d) polished flame-sprayed AlCoCrFeMo HEA coatings [95].

Tian et al. [16] investigated wear performance at varying temperatures using  $\text{Si}_3\text{N}_4$  counterface for atmospheric plasma sprayed AlCoCrFeNiTi HEA coatings on stainless steel 316L substrates. The study was performed at varying temperatures, i.e., 25 °C to 900 °C with a constant normal load. The as-sprayed HEA coatings showed the presence of ordered BCC, disordered BCC, and an FCC phase. The authors reported that there were no changes in phases when tested at 500 °C; however, at elevated temperatures (at 700 °C), CrFe-rich precipitates were found on the wear tracks, indicating a phase transformation from the disordered BCC structure. The CrFe precipitates might have contributed to a reduction in the coefficient of friction and lower wear rates compared to those tested at different temperatures. In general, fine-structured precipitates with small fractions may induce pinning of dislocations by Orowan strengthening, which further contributed towards high hardness and reduction in wear rates. The wear tracks obtained at room temperature and 500 °C showed significant delamination, abrasive grooves, and formation of lips after

testing. The pronounced delamination could possibly be explained by the large plastic flow and adhesive wear. Ex situ analysis of the counterface and their transfer film formations have not been reported by the authors. Nevertheless, the formation of tribofilms was found for the HEA coatings tested at higher temperatures, i.e., 700 °C and 900 °C. The tribofilms consist of compact oxides and mechanically mixed layers—layers that formed due to chemical and processing conditions during wear, which further helped in the reduction in wear rates and coefficient of friction. In a more recent study conducted by Nair et al. [59], the dry abrasive wear behavior (ASTM Standard G65) of new AlCoCrFeMo HEA coatings fabricated using flame spraying and cold spraying techniques was investigated. The comparative study aimed to understand the impact of high temperatures (flame spraying) and low temperatures (cold spraying) on the integrity of the coatings during mechanical loading. The results showed that the flame-sprayed coatings exhibited a spinel-type oxide with BCC phases, while no oxides were observed for the cold-sprayed coatings. The dry abrasion wear study revealed that the flame-sprayed coatings exhibited higher wear resistance, with a brittle mode of wear damage, compared to the cold-sprayed counterparts, which exhibited a ductile mode of wear damage (Figure 14). These findings provide valuable insights into the effects of processing conditions on the mechanical properties of high-entropy alloy coatings.

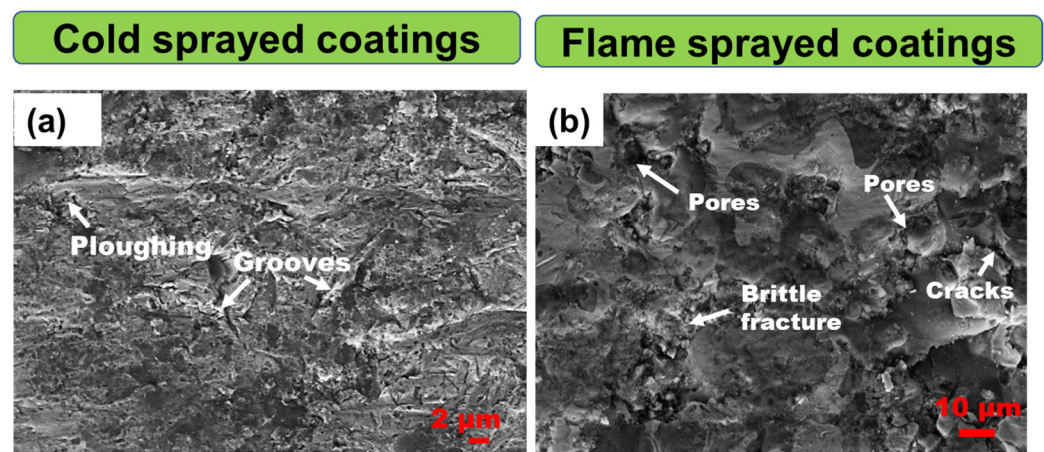


**Figure 14.** Backscattered SEM images of (a) cold-sprayed and (b) flame-sprayed AlCoCrFeMo HEA coatings [59].

A comparative study on FeCoCrNiMo<sub>0.2</sub> HEA coatings using HVOF and APS on a steel substrate was performed by Li et al. [48]. The study concluded that the high fraction of oxides, typically spinel oxides formed for the APS HEA coatings, reduced the wear rates compared to those of HVOF-based HEA coatings. The spinel oxide contents for APS HEA coatings were almost four times higher compared to HVOF HEA coatings. Despite having high fractions of oxides, the hardness values were similar for both HEA coatings. The high fractions of spinel oxides act as a lubricating behavior for the APS HEA coatings, which in turn reduced the wear rates compared to HVOF HEA coatings in an order of magnitude. The dominant wear mechanism involved was abrasion for both the HEA coatings [48].

A few articles also investigated the tribological behavior of cold-sprayed HEA coatings. Yin et al. [38] investigated the wear behavior of high-pressure cold-sprayed FeCoNiCrMn HEA coatings tested at a 5 N load using a WC-Co ball as the counter body. The authors concluded that the significant work hardening ability and grain refinement due to high-velocity impact influenced the wear rate, which was comparatively lower than that of laser-cladded HEA coatings. Similarly, a recent study by Silvello et al. [96] investigated the wear behavior of cold-sprayed and HVOF-sprayed CoCrFeMnNi HEA coatings. The study showed that the cold-sprayed HEA coatings exhibited lower cohesive strength, resulting in higher wear rates compared to HVOF coating. On the other hand, the HVOF coatings

showed low wear rates, which was mainly attributed to their formation of spinel oxides. It was observed that the wear track was characterized by microgrooves and fragmented debris, indicating abrasive wear as the major wear mechanism for the cold-sprayed HEA coatings.

#### 4.2. Corrosion Behaviour

There is a very limited number of studies on the corrosion behavior of thermal-sprayed HEA coatings. Heretofore, AlCoCrFeNi and their derivatives (e.g., Mo and Nb additions) are the studied HEA coatings for corrosion behavior. In all the studied HEA compositions, chromium is the most influential metal to provide material protection against corrosion species due to its stabilized chromium oxide films. It has been reported that the presence of chromium with more than 20 wt.% in the composition provides corrosion protection for HEAs fabricated via arc melting [97]. However, some studies on HEAs claimed that the aluminum addition to CoCrFeNi in high fractions declines the protection capability by depleting chromium from the phases [98]. Still, the debate is ongoing on how the alloy chemical compositions, microstructural, and phase formations influence the corrosion characteristics of HEAs. Furthermore, it should be noted that the reported literature was mainly focused on seawater (may consist of NaCl, CaCl<sub>2</sub>, MgSO<sub>4</sub>, and MgCl<sub>2</sub>) and 3.5 wt.% NaCl as electrolytes. Generally, chloride ions cause severe corrosion damage when compared to an electrolyte containing acidic or alkaline. However, there is a significant research gap on the response of different electrolyte conditions to corrosion performances of thermal-sprayed HEA coatings. More importantly, different chemical compositions of HEAs utilized for thermal spraying have not been studied so far and require further research to understand how the influence of different HEA compositions and their microstructural artifacts could impact the performance under electrochemical damage.

The effect of phase formations (the existence of intermetallics is detrimental to corrosion due to galvanic cell formations) and oxide inclusions in HEA coatings can strongly influence the corrosion current density ( $I_{\text{corr}}$ ), pitting potential ( $E_{\text{pit}}$ ), and eventually, the corrosion rates. Wang et al. [99] investigated the corrosion behavior of (CoCrFeNi)<sub>95</sub>Nb<sub>5</sub> HEA coatings using plasma spraying.  $I_{\text{corr}}$  values showed to be around 7.23  $\mu\text{A}/\text{cm}^2$ , which is lower than that of HEA coatings fabricated using other techniques, highlighting the better corrosion resistance. The presence of stable oxides (i.e., Cr<sub>2</sub>O<sub>3</sub> and Nb<sub>2</sub>O<sub>5</sub>) enhances corrosion resistance for the HEA coatings. Niobium- and chromium-rich interdendrite phases act as micro-galvanic cells, which leads to inferior corrosion resistance. In another study reported the corrosion rates decreased up to 1.6 times by an increase in the molybdenum additions in AlCoCrNiMo<sub>x</sub> ( $x = 0.5$  and 1) HEAs fabricated by HVOF [100]. These HEA coatings showed approximately 2.4 times better corrosion performance than that of traditional NiCrSiB coatings under 3.5 wt.% NaCl solution. More recent study by Liu et al. [101] reported that the AlCoCrFeNiTa deposited by means of HVAF technique showed a dense hypo-eutectic structure, with a single-phase solid solution. The corrosion behavior exhibited excellent pitting resistance compared to SUS 304 steel under 3.5 wt.% NaCl solution.

Mu et al. [57] investigated the corrosion performance of AlCoCrFeNi HEA fabricated by means of APS. They utilized different power sources to study their effects on corrosion behavior. The coatings with high voltage exhibited low  $I_{\text{corr}}$  values, highlighting the better corrosion resistance. The electrochemical impedance spectroscopy (EIS) study revealed the high charge transfer resistance ( $R_{\text{ct}}$ ) for the HEA coatings fabricated at high voltage, which indicated better passivation resistance. X-ray photoelectron spectroscopy (XPS) showed the presence of species including Al<sub>2</sub>O<sub>3</sub>, Co<sub>3</sub>O<sub>4</sub>, Cr(OH)<sub>3</sub>, Fe<sub>2</sub>O<sub>3</sub>, Fe<sub>2</sub>O<sub>4</sub>, FeO, NiO, and bound water (H<sub>2</sub>O) on the corroded surfaces, where the presence of bound water improved the corrosion performance of HEA coatings. Meghwal et al. [68] investigated the AlCoCrFeNi HEA coatings using APS in comparison with stainless steel 316L under seawater conditions. The HEA coatings showed slightly higher  $I_{\text{corr}}$  values (0.83  $\mu\text{A}/\text{cm}^2$ ) compared to that of stainless steel 316L (0.26  $\mu\text{A}/\text{cm}^2$ ), as shown in Figure 15a. Micrographs of the corroded surface revealed the formation of the pores and pits for the HEA coatings, which indicates

the general and localized corrosion attacks (Figure 15b,c). Stainless steel 316L is known as a corrosion-resistant material due to its  $\text{Cr}_2\text{O}_3$  stabilization, which acts as the barrier to selective and localized corrosion. On the other hand, the microstructural inhomogeneities and porosities act as preferential sites that lead to poor corrosion resistance for the HEA coatings. The multiphase formed with oxides may act as micro-galvanic cells, which also increased the  $I_{\text{CORR}}$  values compared to stainless steel 316L.

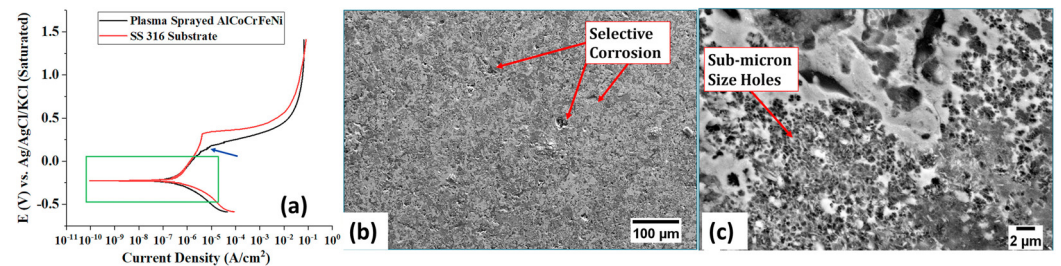


**Figure 15.** (a) Potentiodynamic polarization curves of APS AlCoCrFeNi HEA coatings and SS 316L and (b,c) depict the corroded HEA surfaces [68].

More recently, Nair et al. [59] investigated the electrochemical corrosion of newly developed AlCoCrFeMo coatings deposited by means of flame spraying and low-pressure cold spraying techniques using a 3.5 wt% NaCl solution. The authors reported that the lack of oxide contaminations and reduced porosity level contributed to an improvement in the corrosion resistance (approximately two times), low corrosion current density, and high passivation capability for the cold-sprayed coatings compared to those of flame-sprayed counterparts, as shown in Figure 16. The presence of oxides inclusions during oxidation in-flight, which has different chemical composition gradients, increased the corrosion rates for the flame-sprayed HEA coatings due to the formation of micro-galvanic cells. Furthermore, the porosity level was higher in the case of flame-sprayed HEA coatings, which may act as preferential sites for the electrolyte to pass through, resulting in high corrosion rates. The comparative studies of the corrosion current density indicated that the thermal-sprayed HEA coatings showed better performance compared to that of the HEA coatings fabricated using different manufacturing routes when tested under 3.5 wt% NaCl solution [59,96,97,99,102–105], as shown in Figure 17.

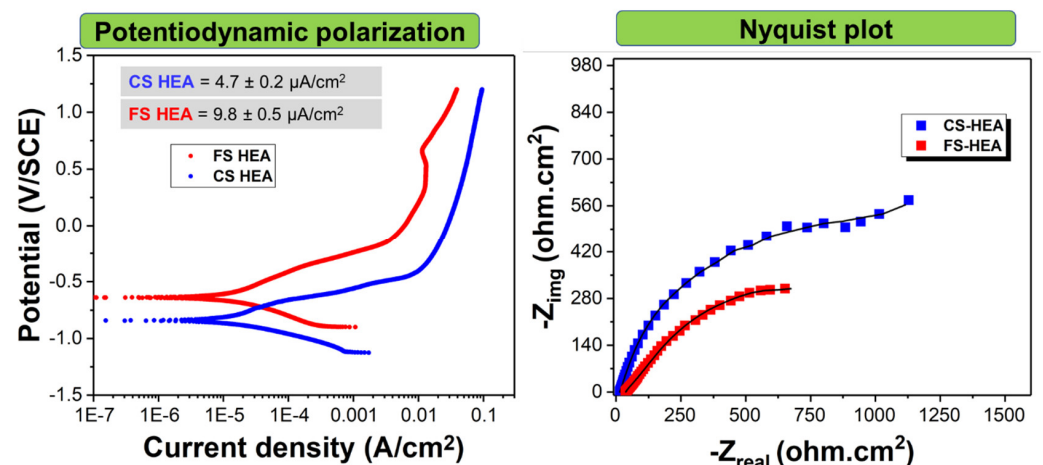


**Figure 16.** Electrochemical corrosion studies representing potentiodynamic polarization curves and Nyquist plot of flame-sprayed and cold-sprayed AlCoCrFeMo HEA coatings. The figure indicates that the cold-sprayed HEA coatings showed better corrosion performance compared to flame-sprayed HEA coatings [59].

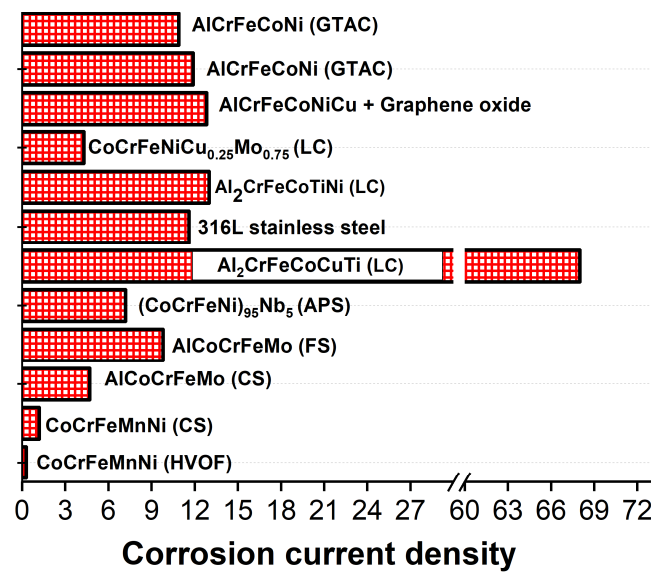


**Figure 17.** A comparative assessment of corrosion current density for thermally sprayed HEA coatings with other HEA coatings fabricated using different methods under 3.5 wt% NaCl solution [59,96,97,99,102–105]. The thermal-sprayed HEA coatings showed lower corrosion rates compared to stainless steel 316L and other HEA coatings. GTAC is gas tungsten arc cladding, CS is cold spraying, FS is flame spraying, HVOF is high-velocity oxy-fuel, APS is air plasma spraying, and LC is laser cladding.

#### 4.3. Oxidation Behaviour

Although the performance of HEA coatings against corrosion was better than traditional materials, studies on the oxidation behavior of thermal-sprayed HEA coatings were also shown promise. The literature investigated oxidation response on thermal-sprayed HEA coatings that were similar to that of electrochemical corrosion. The studies on oxidation response are crucial for thermal-sprayed HEA coatings that can be served in elevated temperature applications. Hsu et al. [29,106,107] fabricated HEAs based on the family of non-equimolar  $\text{NiCo}_{0.6}\text{Fe}_{0.2}\text{Cr}_x\text{Si}_z\text{AlTi}_y$  coatings using APS, HVOF, and warm spraying (modified HVOF technique). The alloy coatings development strategy aiming at achieving a clearly beneficial property combination, which is required for the insertion of new high-temperature coatings, can be summarized as follows. Chromium and titanium, in addition to aluminum, should ensure the formation of protective oxide scales. The addition of silicon also favors providing oxidation protection with chromium and titanium constituent elements. All the HEA coatings were compared to traditionally utilized  $\text{MCrAlY}$  ( $\text{M} = \text{Ni}$  or  $\text{Co}$  and/or their combinations) coatings, respectively. The  $\text{MCrAlY}$  coating was typically used for bond coating for thermal barrier applications. Most of the oxidation studies were performed at a temperature of 1100 °C.

The first study conducted by Hsu et al. [29] was fabricated by using APS-based HEA coatings with an increase in chromium content, and the result showed a similar oxidation response compared to that of  $\text{NiCrAlY}$  coatings after the completion of 150 h. The steady-state regime was found for the HEA coatings after 100 h, indicating stable oxide scales. The mixed Ti-Cr-Al oxides and  $\text{Al}_2\text{O}_3$  are the major contributing thermally grown oxides (TGO) to provide oxidation resistance. The next study conducted by Hsu et al. [106] used two HEA overlay coatings with varying chromium and titanium in  $\text{NiCo}_{0.6}\text{Fe}_{0.2}\text{Cr}_{1.3}\text{SiAlTi}_{0.2}$  and  $\text{NiCo}_{0.6}\text{Fe}_{0.2}\text{Cr}_{1.5}\text{SiAlTi}$  fabricated using HVOF, APS, and warm spraying (modified HVOF technique), respectively. In this case, the oxidation time increased to 336 h. A steep rise in weight gain was observed for all the HEA coatings compared to  $\text{MCrAlY}$  coatings, indicating inferior oxidation performance. The weight gain showed a sudden rise after 250 h for the HEA coatings. Among the HEA coatings, warm-sprayed coatings showed the highest oxidation resistance, which is mainly due to the non-porous oxide scales. The

subsurface layer confirmed the Ti-Cr-Al and  $\text{Al}_2\text{O}_3$  are the oxide scales formed for all the HEA coatings. Another study was reported by adding Si in  $\text{NiCo}_{0.6}\text{Fe}_{0.2}\text{CrSi}_{0.2}\text{AlTi}_{0.2}$  HEA overlay coatings using APS and HVOF, respectively [107]. The oxidation studies were performed in comparison with MCrAlY (Co-30Ni-21Cr-15Al-0.5Y) coatings. The weight gain showed a sharp rise until 50 h, followed by steady-state conditions for the HEA coatings, whereas the MCrAlY coatings showed a steep rise until 168 h. The results conclude that the oxidation resistance was similar to that of MCrAlY coatings at 1100 °C.

The  $\text{Al}_2\text{O}_3$  and  $\text{Cr}_2\text{O}_3$  serve as protective oxide scales, which yield better oxidation resistance for the HEA coatings. For instance, two HEA  $\text{AlSiTiCrFeCoNiMo}_{0.5}$  and  $\text{AlSiTiCrFeNiMo}_{0.5}$  coatings showed the first increase in oxidation resistance from 900 to 1000 °C and declines at 1100 °C, which is due to the formation of unstable  $\text{TiO}_2$  scales at the outer layer. Among all the temperatures, both the HEA coatings showed better oxidation performance at 1000 °C, which is attributed to their strong chromium oxide scales [49]. Another study by Anupam et al. [37] reported  $\text{Al}_2\text{O}_3$  protective oxides are the main contributing factors for oxidation resistance for the cold-sprayed  $\text{AlCoCrFeNi}$  coatings while performed at 1100 °C for 100 h. Recently, Xu et al. [108] investigated the oxidation performance of  $\text{FeCoCrNiMn}$  fabricated using cold spraying at 700–900 °C and compared it with their bulk forms. The cold-sprayed  $\text{CoCrFeMnNi}$  showed a similar oxidation rate ( $k_p = 0.0208 \text{ mg}^2 \text{ cm}^{-4} \text{ h}^{-1}$ ) compared to as-cast HEA ( $k_p = 0.0197 \text{ mg}^2 \text{ cm}^{-4} \text{ h}^{-1}$ ) at 700 °C but higher at high temperatures. The multi-oxide scales were observed on the sublayer, which includes  $\text{Mn}_2\text{O}_3$  outer layers, and Mn-Cr spinel layers along with  $\text{Cr}_2\text{O}_3$  inner layers, respectively, at 700 and 800 °C. The significant grain boundaries promote the manganese outer diffusion, which results in the formation of manganese oxide scales, which was not found for the as-cast HEAs. These studies give a new opportunity to explore detailed studies regarding the oxidation response in thermal-sprayed HEA coatings and can be potentially transformative.

## 5. Types of HEA Coatings and Their Potential Applications

### 5.1. Refractory-Based High-Entropy Alloys (RHEAs) for High Temperature Applications

Refractory-based HEAs (RHEAs) have gained significant attention in the materials science community due to their prospective properties at elevated temperatures. Despite having high-temperature strength and oxidation resistance, the limited capability of nickel superalloys to perform at temperatures above 1000 °C has always been a challenge. The features of RHEAs in terms of resistance to high-temperature softening and high melting point that can sustain more than 2000 °C outperform the superalloys reported by the literature [109–112]. Furthermore, the high-temperature strength and ductility, along with superior oxidation and corrosion resistance of RHEAs at elevated temperatures, increased the demand to focus on thermal barrier coatings. However, no reports have been provided for RHEAs fabricated using thermal spray technologies so far. Grouping the elements with refractory and transition-based metals offers excellent properties for high-temperature strength and oxidation [112–114]. Employing thermal spraying technologies for HEAs may enable a breakthrough for applications that demand elevated temperatures rather than bulk counterparts because of its versatility and low manufacturing cost.

However, till now, more than 120 refractory-based high-entropy materials have been developed using various technologies due to their exceptional high-temperature properties. Primarily, RHEAs form as BCC phases, mostly with single phase BCC structure with high strength at room and elevated temperature (even at the high temperature of 1600 °C) and high resilience to thermal softening because of the slower diffusion kinetics [61] and thus capable as coatings for high-temperature gas turbine regions in aerospace sectors. More importantly, the combination of refractory (Ta, Nb, etc.) and transition metals (Al, Cr, Mo) provide an excellent combination of high melting point and oxidation and corrosion resistance, enabling them to use for high-temperature applications replacing superalloys. Recently, Gorr et al. [112,113,115–117] proposed novel RHEAs based on the x-Mo-Cr-Ti-Al (x = W, Nb, Ta) alloy system developed by arc-melting and annealing. The alloy

development strategy aiming at achieving a clearly beneficial property combination, which is required for the insertion of new high-temperature materials, can be summarized as follows. The addition of tungsten, niobium, tantalum, and molybdenum should provide a high melting point, high-temperature strength, and creep resistance. Additions of titanium and aluminum should guarantee reasonable density, while chromium, in addition to aluminum, should ensure the formation of protective oxide scales. While the equiatomic alloy W-Mo-Cr-Ti-Al possesses a single-phase BCC microstructure, the substitution of tungsten by niobium causes the formation of the ordered Laves and A15 phases [112,117]. In addition to the BCC and the Laves phases, the ordered B2 phase becomes dominating in the Ta-Mo-Cr-Ti-Al alloy [116]. Furthermore, the Ta-Mo-Cr-Ti-Al alloy shows very high oxidation resistance. Oxidation experiments yielded values of the mass gain of less than 1 mg/cm<sup>2</sup> and ~3 mg/cm<sup>2</sup> at 1000 and 1100 °C, respectively, after 48 h [115,116]. The formation of the protective Al<sub>2</sub>O<sub>3</sub> oxide scale along with CrTaO<sub>4</sub> explains the high oxidation resistance of the Ta-Mo-Cr-Al-Ti alloy [115]. The remarkable properties of RHEAs, such as high melting point, high hardness, and oxidation resistance, are beneficial for harsh environments and, thus, suitable for the components used in gas turbines. However, the exploration of RHEAs in conjunction with thermal spraying technologies for high-temperature applications has not been carried out to date, and further research is required.

### 5.2. Transition-Based High-Entropy Alloys for Aerospace Applications

For aeroengines, static and dynamic seals are vital components that help to prevent the leakage associated with gases and fluids. Figure 18 shows a typical cross-section of aeroengines, wherein static and dynamic seals are represented in blue regions [118]. Indeed, the seals are used in different sections of aero engines in order to control oil leakages from the gearboxes, and hence, static and dynamic seals comprise a wide range of material designs that are operatable at different temperature regions. Nonetheless, due to the severe operating conditions, engine seals undergo pronounced vibrations relative to the interfaces, which may cause high friction and wear, and thus, reducing their efficiency to control the leakages [119]. The high friction and wear are mainly associated with traditional material coatings that are unable to withstand such high operating conditions. There are ongoing studies in order to assimilate advanced engineering materials that are capable to withstand high friction and wear operating in different working environments, especially in the high-temperature sections. Thermal-sprayed HEA coatings have shown promising wear behavior at elevated temperatures, which can be a potential candidate for such extreme applications. The lightweight nature and superior specific strength at high temperatures offered by AlCoCrFeNi HEA compositions may be a preferred choice of materials over traditional materials utilized for aerospace seal applications [120]. However, further research is required to understand how the different temperatures influence the wear performance of different chemistries of thermal-sprayed HEA coatings.

Thermal barrier coatings are utilized to protect gas turbine components from extreme temperatures. The thermal barrier coatings consist of a metallic bond coat as the first layer and ceramic coating (typically yttria-stabilized zirconia) as the top layer coatings. Typically, MCrAlY is used as metallic bond coating as these coatings provide reasonable oxidation performance due to the formation of Al<sub>2</sub>O<sub>3</sub> oxide scales, acting as a protective shield for base materials. Most of the transition-based HEAs have shown exceptional properties due to their sluggish diffusion kinetics and high configurational entropy effect [121]. Aluminum and its oxide counterparts formed are the protective scales preventing oxidation; however, utilizing the high-temperature deposition techniques reduces the aluminum content in the HEA coatings, reported by Ang et al. [20]. More specifically, a deposition technique that can work under low-temperature is a feasible approach to developing HEA coatings that can provide protective oxide films from further oxidation. Cold-sprayed and high-velocity air fuel HEA coatings as bond coatings for thermal barrier systems have not been explored to date and open a new research direction to explore transition-based HEA coatings.

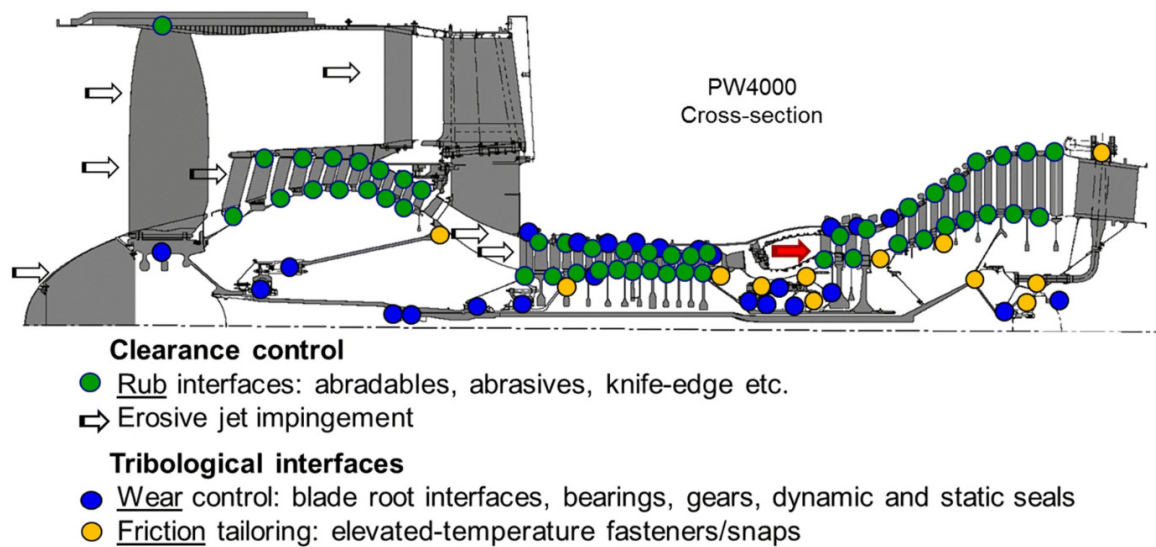


**Figure 18.** Typical seals and their locations in gas turbine engines [118].

### 5.3. High-Entropy Carbides

High-entropy-driven materials provide a challenging aspect to design materials based on certain applications. Although transition and refractory metals endow a scope in terms of structural materials for harsh environments, the researchers extend their focus to designing and developing carbides from the group of IVB, VB, and VIB transition metals are known as high-entropy carbides (HECs) [122–125]. The most attractive features of HECs are their ability to persist in single-phase structures at extreme temperatures and local chemical environments. The advantages of slow diffusion kinetics and distorted lattices favor the HECs to provide thermal protection, improved strength and hardness, and better oxidation resistance. Furthermore, the HECs are defined as materials with ultra-high melting points (>3000 °C), which increase their demand in extreme operational conditions in structural applications such as rocket nozzles and nuclear reactors. The plausible elements based on the vulnerability of the applications should have to be explored to develop high-entropy-driven carbides.

### 5.4. High-Entropy Oxides

The rapid development of high-entropy materials and their strong correlations between compositions and properties opens a new window to study the prospects of these materials in the form of oxides. High-entropy oxides (HEOs) are an emerging branch of high-entropy materials, which can fulfill the requirements in applications such as catalyst, dielectrics, and magnetic properties and in particular for top coating for thermal barrier coatings (TBC) [126–131]. The distinct nature of anion and cation sublattices in HEOs bestow better solubilities and stabilizations. Although the field of research based on HEOs is in its inception, the understanding of developing the HEOs by means of thermal spraying is challenging. The structural formation and properties of thermal spraying (i.e., plasma spraying) HEO coatings should have to be explored to expand their research for applications such as catalysis, water splitting, thermal protection, supercapacitors, and thermoelectric and thermal barrier coatings. HEOs developed through the arc melting process had been proven for their magnetic [127,128] and energy storage [129,132] applications, and hence, the thermal-sprayed HEO coatings may provide a fascinating research topic in the near future.

### 5.5. High-Entropy Alloy Composites

Metal matrix composites (MMCs) have widely been studied for many industrial applications due to their high hardness and excellent strength with optimum ductility and toughness [80,133,134]. A number of secondary particles as reinforcement, typically ceramics, are incorporated into the metal matrix to enhance the inherent features of the composite structures that can be implemented in various industrial sectors. Considering the attractive properties attained through these composites, HEAs are used as a metal matrix with ceramic reinforcements (i.e., TiC, SiC, WC, Al<sub>2</sub>O<sub>3</sub>, TiN) developed through different techniques such as induction melting [73,135], plasma cladding [136], microwave processing [85,86], spark plasma sintering (SPS) [137–139] and additive manufacturing (AM) [140,141]. Thus, a new family of MMCs arose in the field of HEAs known as high-entropy composite alloys (HEACs). Together with thermal spraying and cold spraying technologies, HEACs can provide an excellent opportunity to break the bottleneck problems associated with wear and corrosion. One such example is the fatigue fracture (due to cyclic loading of bubble implosions) and plastic deformation failures when exposed to cavitation erosion damage. Therefore, the concurrent high strength and toughness interactions are significant in controlling cavitation damage due to bubble implosions. To the best of the authors' knowledge, only one group investigated the cavitation erosion-corrosion response on AlCoCrFeNi HEAs fabricated through the HVOF technique [62]. HEA coatings showed 3.5 times lower cumulative mass loss (CML) than conventional steel (06Cr13Ni5Mo) after 24 h of testing. The presence of BCC phases in HEA coatings enhances the hardness due to solid solution strengthening that controls damage due to bubble implosions. Lamellar spalling and interlaminar cracks are the dominant damage mechanisms observed after testing. Different HEACs can be designed by tailoring the chemical compositions and with the addition of reinforcement that can be fabricated using deposition techniques depending on the vulnerability of severe degradations such as wear, corrosion, tribo-corrosion, and oxidation.

### 5.6. Perspectives on Other Applications of Thermal-Sprayed HEA Coatings

By varying their chemical compositions, high-entropy alloys (HEAs) can offer a range of potential benefits in multifunctional roles, such as catalysis and energy applications, thereby opening up new possibilities for these materials. The governing factors, including high configurational entropy and severe lattice distortions, enable HEAs to perform as a catalyst. The high configurational entropy promotes a disordered environment that may increase the surface area of the catalyst, whilst the severe distortion in the lattice structure enables structural defects. These two structural characteristics accelerate the rate of catalytic reactions by increasing the number of active sites, which facilitate HEAs to perform as effective catalysts. The most promising attribute of HEAs is the meticulous material selections and their property tuning by varying the chemical compositions in atomic length, which helps to modify the crystal structures to mold them as a feasible catalysis. Employing the established thermal spraying manufacturing routes is considered a top-notch approach to fabricating catalytic HEAs. However, to the best of the author's knowledge, the utilization of HEAs through thermal spraying is still lacking. Being the vast compositional space of HEAs, designing new-generation catalytic HEA coatings would be challenging and require high-throughput screening using computational tools such as machine learning.

Recent studies show the potential features of arc-melted HEAs to use in orthopedic implant applications in terms of hip and knee replacements [142–146]. Although the demand for bio implant materials is increasing due to automobile accident rates and sports injuries, premature failure due to localized corrosion in a highly aggressive physiological environment becomes a long-term issue for using traditional materials. The presence of toxic ions is another problem in conventional materials such as stainless steel, which leads to allergic reactions in the human body. The distinguished microstructural features of HEAs, along with anti-wear and anti-corrosion properties, endow the possibility of HEAs

to use as a novel type of bioimplant material [147,148]. Perumal et al. [147] investigated MoNbTaTiZr alloy through arc-melting and studied the biocorrosion. According to the authors, the dual-phase structure that reduces elemental heterogeneity is a governing factor in enhancing the biocorrosion resistance and cellular response compared to stainless steel 316L. Nonetheless, the field of research is highly unexplored in terms of HEA coatings, and the potential benefits of HEAs can provide a helpful hand to develop bioimplant coatings with improved wear and corrosion resistance, excellent strength-weight ratio, and biocompatibility. The perspective for future studies associated with thermal spray HEA coatings would invigorate the interests of researchers to focus extensively on the directions of orthopedic implants.

Radiation damage in the nuclear sector is another challenging area of research, where the structural material damage is due to the high-dose of radiation at high temperatures. The traditional materials for nuclear reactors are unable to overcome high-dose neutron irradiations, which eventually results in material embrittlement, hardening, and failure. The salient features of HEAs with topological lattice distortion capability between constituent elements can be able to provide a self-healing ability to encounter the high radiation dose. The findings of arc-melted HEAs showed an excellent irradiation response compared to traditional materials [149,150]. The high compositional complexity of HEAs, along with the more disordered structure, inhibits the defects to pass through the materials, hence reducing the overall damage caused by radiation. Moreover, solid solution phases and lattice distortion offered by HEAs enable high lattice defects (i.e., dislocations), which absorb and reduce the damage due to radiation [149,150]. This expands the possibility of such a study in the field of HEA coatings through thermal spray manufacturing routes.

Thermal-sprayed high-entropy alloy coating properties can be further enhanced through targeted strategies in order to create next-generation materials with unique properties. One of the main advantages of HEAs is that they provide numerous possibilities in designing alloys, including the combinations of transition metals, refractory elements, and ceramics. For achieving favorable phase formations and desired mechanical properties such as strength and toughness, the selection of plausible alloying elements is paramount. Recently, researchers used the CALPHAD approach for designing numerous high-entropy alloys with different variations of alloying elements and predicted their phase formations, which in turn can identify the strengthening mechanisms of HEAs. For instance, Guo et al. [151] used the CALPHAD approach coupled with experimentation results to design and develop precipitation-strengthened  $(\text{FeCoNi})_{95}\text{Al}_{2.5}\text{Ti}_5$  high-entropy alloys. Thermo-Calc software with the TTN18 database was used to predict the phase formations of the HEA.

Their studies validated that the formation of  $\text{Ni}_3\text{Al}$  based  $\gamma'$  nanoprecipitates was found for the HEAs using Thermo-Calc software and transmission electron microscopy. Indeed, CALPHAD has emerged as a profound tool for predicting the phases, microstructure, and material properties of numerous high-entropy alloy systems. CALPHAD, in conjunction with the machine learning approach, is an emerging trend for designing numerous plausible HEA systems that can pave the way for better mechanical properties. Such an approach corroborates the research significance in predicting the alloying elements in thermal-sprayed HEA coatings. However, the evolution of oxide phases is a common microstructural artifact in thermal-sprayed HEA coatings due to their oxygen-sensitive elements (typically Al, Cr, Mo, Fe, etc.). Therefore, there is a strong need to perform research in predicting the oxide formations using the CALPHAD-aided approach for high-entropy alloys by means of thermal spraying technologies. Table 3 provides a summary of how the phases behave in response to the composition of high entropy alloys fabricated using various deposition techniques.

**Table 3.** Different high-entropy alloy compositions and their phase formations and porosity levels according to deposition techniques.

| High Entropy Alloy Coatings  | Feedstock Routes     | Substrates                              | Deposition Routes | Phases   | Porosity (%) | Ref.  |
|--|----------------------|---|-------------------|--|--------------|-------|
| AlCoCrFeNi   | MA                   | Mild steel                              | APS               | BCC + FCC + oxides                                   | 9.5 ± 2.3    | [20]  |
|  | Gas atomized         |   | APS               | BCC and FCC  | -            | [51]  |
|  | Gas atomized         | AISI 1045 steel                         | APS               | BCC and B2   | -            | [56]  |
|  | MA                   | Low carbon steel                        | APS               | BCC + FCC + oxides                                   | -            | [57]  |
|  | MA                   | Mild steel                              | HVOF              | B2   | -            | [61]  |
|  | MA                   | Mild steel                              | HVAF              | B2   | -            | [61]  |
|  | Water atomized       | 06Cr13Ni5Mo martensitic stainless steel | HVOF              | FCC and BCC  | -            | [62]  |
|  | MA                   | SS 316L                                 | APS               | Al-rich oxides + AlCrFe oxides + Al-depleted regions | -            | [68]  |
| Al <sub>0.5</sub> CoCrFeNi <sub>2</sub>                              | Gas atomized         | SS 304                                  | APS               | FCC  | -            | [69]  |
| AlCoCrFeNiTi   | MA                   | S235 steel                              | APS               | BCC and FCC  | -            | [14]  |
|  | Gas atomized         | S235 steel                              | APS               | BCC and FCC  | -            | [14]  |
|  | MA                   | SS 316                                  | APS               | BCC and oxides                                       | -            | [16]  |
|  | Gas atomized         | S235 steel                              | HVOF              | BCC + B2 + A12                                       | -            | [78]  |
| Al <sub>0.6</sub> CoCrFeNiTi   |                      | A572 steel                              | HVOF              | BCC  | -            | [79]  |
| MnCoCrFeNi   | MA                   | Mild steel                              | APS               | BCC + FCC + oxides                                   | 7.4 ± 1.3    | [20]  |
|  | Gas atomized         | SS 316L                                 | Detonation        | FCC and oxides                                       | -            | [63]  |
|  | Gas atomized         | SS 304                                  | APS               | FCC  | -            | [152] |
| FeCoCrNiMo <sub>0.2</sub>  | Gas atomized         | Low carbon steel                        | APS               | FCC and oxides                                       | -            | [70]  |
|  | Gas atomized         | Low carbon steel                        | HVOF              | FCC and oxides                                       | -            | [70]  |
| WC-10Co/AlCoCrFeNi   | Water atomized       | 06Cr13Ni5Mo martensitic stainless steel | HVOF              | FCC + BCC  | -            | [72]  |
| Ni60/AlCoCrFeNiTi  | MA + gas atomized    | SS 316                                  | APS               | BCC and oxides                                       | -            | [15]  |
| Ag/Al <sub>0.2</sub> CrCo <sub>1.5</sub> FeNi <sub>1.5</sub> Ti      | Mechanically blended | Carbon steel                            | APS               | BCC + B2 + FCC + Cr Carbides                         | -            | [69]  |
| Al <sub>2</sub> O <sub>3</sub> -13 wt.% TiO <sub>2</sub> /MnCoCrFeNi | Gas atomized         | Mild steel                              | APS               | FCC and oxides                                       | -            | [74]  |
| Nano oxides/MoCrCoFeNi   | Gas atomized         | -                                       | APS               | BCC + FCC + oxides                                   | -            | [57]  |
| AlCoCrFeNiSi   | MA                   | SS 316                                  | APS               | B2 and BCC   | -            | [58]  |
| AlCoCrFeNi   | MA                   | Ni-base super alloy                     | CS                | BCC  | 7            | [37]  |
| MnCoCrFeNi   | Gas atomized         | Al 6082 alloy                           | CS                | FCC  | -            | [38]  |
| AlCoCrFeNiTi   | MA                   | Steel                                   | CS                | B2 + TiC + σ   | 0.5 ± 0.18   | [47]  |
| MnCrFeNi   | Gas atomized         | Fe52 steel                              | CS                | BCC  | -            | [36]  |

Table 3. Cont.

| High Entropy Alloy Coatings   | Feedstock Routes                 | Substrates | Deposition Routes | Phases                     | Porosity (%) | Ref.  |
|---|----------------------------------|------------|-------------------|----------------------------|--------------|-------|
| MnCrFeNi  | Gas atomized                     | Fe52 steel | CS                | BCC                        | -            | [36]  |
| Ni <sub>0.2</sub> Co <sub>0.6</sub> Fe <sub>0.2</sub> CrSi <sub>0.2</sub> AlTi <sub>0.2</sub> | Gas atomized                     | SS 304     | APS               | BCC and Cr <sub>3</sub> Si | -            | [54]  |
| NiC <sub>0.6</sub> Fe <sub>0.2</sub> CrSiAlTi <sub>0.2</sub>                                  | Gas atomized                     | SS 304     | APS               | BCC and Cr <sub>3</sub> Si | -            | [54]  |
| Ni <sub>0.2</sub> Co <sub>0.6</sub> Fe <sub>0.2</sub> Cr <sub>1.5</sub> SiAlTi <sub>0.2</sub> | Gas atomized                     | SS 304     | APS               | BCC and Cr <sub>3</sub> Si | -            | [54]  |
| CrMnFeCo  | -                                | -          | APS               | FCC                        | 2.9          | [42]  |
| NiCo <sub>0.6</sub> Fe <sub>0.2</sub> Cr <sub>1.5</sub> SiAlTi <sub>0.2</sub>                 | Arc melting + mechanical milling | -          | APS               | BCC                        | 1–5          | [107] |
| Al <sub>0.6</sub> TiCrFeCoNi  | Gas atomized                     | -          | HVOF              | BCC                        | 1.68         | [79]  |
| Ni <sub>0.2</sub> Co <sub>0.6</sub> Fe <sub>0.2</sub> CrSi <sub>0.2</sub> AlTi <sub>0.2</sub> | Arc melting + mechanical milling |            | HVOF              | BCC                        | 2.8 ± 0.5    | [29]  |
|   |                                  |            | APS               | BCC                        | 4.3 ± 0.5    | [29]  |

## 6. Conclusions

In recent years, the utilization of high-entropy alloy (HEA) coatings through thermal spraying have become widespread due to their versatile microstructures and advantageous properties. Enhancing the resistance of these alloys to surface degradation would make them highly attractive for a broad range of commercial applications. However, there is still considerable scope for advancement in this area. Therefore, research on future directions for thermal-sprayed HEA coatings could concentrate on the following:

1. HEA coating fabrication: Although several thermal-sprayed HEA coatings have been reported, there is a need to investigate HEA compositions utilizing high-velocity air fuel (HVOF) and cold spraying (CS) deposition techniques. Researchers can develop HEA coatings using these methods and study their microstructure and phase evolution, along with post-treatment methods for specific service conditions;
2. Quantitative mechanical properties for extreme environments: While the previous studies of HEA coatings have focused primarily on micro-hardness, the coatings' reliability under various loading conditions also depends on other mechanical properties such as yield strength, ultimate strength, ductility, toughness, strain hardening, and elastic modulus. However, these properties have not been adequately explored to correlate them with mechanical damage due to wear;
3. Parametric optimization: The parameters for thermal spraying should be optimized to produce high-quality HEA coatings that exhibit desirable mechanical properties such as strength and toughness. Researchers should explore various processing techniques and optimize parameters such as feedstock feed rate, spray distance, gas flow rates, etc, to enhance the coatings' reliability. One area of research could be using machine learning algorithms to optimize the process parameters for the thermal spraying of HEA coatings;
4. Unraveling different HEA classifications through thermal spraying: To identify their potential for industrial applications, researchers should explore different HEA systems. One such example is refractory-based high-entropy alloys and high-entropy oxides for bond and top coatings for thermal barrier coatings in high-temperature applications;
5. Investigation of microstructure and phase evolution: A comprehensive understanding of the microstructure and phase evolution of HEA coatings is essential for the development of advanced coatings with optimal properties. Researchers can undertake a detailed investigation of the microstructure and phase evolution of HEA coatings at different stages of the coating's life cycle, including during the spraying process, post-treatment, and under service conditions. By analyzing the evolution of the coating's

microstructure and phases over time, researchers can gain insights into the underlying mechanisms governing the coating's behavior and identify opportunities for improving the coating's performance;

6. Evaluation of wear properties: HEA coatings have demonstrated potential for wear applications. However, further research is required to understand their ex-situ mechanism for tribological interfaces and under extreme environmental conditions;
7. Evaluation of corrosion properties: HEA coatings exhibit good corrosion resistance in seawater and sodium chloride electrolyte conditions. Nonetheless, studies on corrosion properties under different electrolyte conditions, such as HCl and H<sub>2</sub>SO<sub>4</sub>, are limited.

The versatile properties of thermal-sprayed HEA coatings make them highly attractive for a multitude of industries, such as aerospace, automotive, and biomedical. To harness the full potential of HEA coatings in various applications, researchers can delve into their unique characteristics and develop tailored coatings that precisely cater to the specific requirements of each industry.

**Author Contributions:** R.B.N. and R.S. conceived and designed the layout of the review paper; R.B.N. analyzed strengthening mechanisms, corrosion, oxidation, and types of HEAs and their potential application sections; R.B.N. and R.S. analyzed the wear section; S.M.J. analyzed the feedstock section; W.W. analyzed the microstructure section; A.M., J.M., Y.Z. and P.S. reviewed critically and revised the manuscript; A.M., J.M. and P.S. funding acquisition, R.B.N. and R.S. wrote the manuscript. All authors have read and agreed to the published version of the manuscript.

**Funding:** The authors gratefully acknowledge Natural Science and Engineering Research Council of Canada (Award Number: RGPIN-2018-04298) for their funding support for this project.

**Institutional Review Board Statement:** Not applicable.

**Informed Consent Statement:** Not applicable.

**Data Availability Statement:** The data presented in this study are available from the corresponding authors upon request.

**Conflicts of Interest:** The authors declare no conflict of interest.

## References

1. Cantor, B.; Chang, I.; Knight, P.; Vincent, A. Microstructural development in equiatomic multicomponent alloys. *Mater. Sci. Eng. A* **2004**, *375*, 213–218. [[CrossRef](#)]
2. Yeh, J.W.; Chen, S.K.; Lin, S.J.; Gan, J.Y.; Chin, T.S.; Shun, T.T.; Tsau, C.H.; Chang, S.Y. Nanostructured high-entropy alloys with multiple principal elements: Novel alloy design concepts and outcomes. *Adv. Eng. Mater.* **2004**, *6*, 299–303. [[CrossRef](#)]
3. Tsai, M.-H.; Yeh, J.-W. High-entropy alloys: A critical review. *Mater. Res. Lett.* **2014**, *2*, 107–123. [[CrossRef](#)]
4. Gorsse, S.; Couzinié, J.-P.; Miracle, D.B. From high-entropy alloys to complex concentrated alloys. *C. R. Phys.* **2018**, *19*, 721–736. [[CrossRef](#)]
5. Miracle, D.B. Critical Assessment 14: High entropy alloys and their development as structural materials. *Mater. Sci. Technol.* **2015**, *31*, 1142–1147. [[CrossRef](#)]
6. Murty, B.S.; Yeh, J.-W.; Ranganathan, S. *High-Entropy Alloys*; Elsevier: New York, NY, USA, 2014.
7. Wang, J.; Zhang, Z.; Dai, H.; Fujiwara, H.; Chen, X.; Ameyama, K. Enhanced corrosion resistance of CoCrFeMnNi high entropy alloy using heterogeneous structure design. *Corros. Sci.* **2022**, *209*, 110761. [[CrossRef](#)]
8. Gao, M.C.; Yeh, J.-W.; Liaw, P.K.; Zhang, Y. *High-Entropy Alloys: Fundamentals and Applications*, 1st ed.; Springer: Berlin/Heidelberg, Germany, 2016.
9. Tejero-Martin, D.; Rad, M.R.; McDonald, A.; Hussain, T. Beyond traditional coatings: A review on thermal-sprayed functional and smart coatings. *J. Therm. Spray Technol.* **2019**, *28*, 598–644. [[CrossRef](#)]
10. Zhang, H.; Chen, X.; Gong, Y.; Tian, Y.; McDonald, A.; Li, H. In-situ SEM observations of ultrasonic cavitation erosion behavior of HVOF-sprayed coatings. *Ultrason. Sonochem.* **2020**, *60*, 104760. [[CrossRef](#)] [[PubMed](#)]
11. Galedari, S.A.; Mahdavi, A.; Azarmi, F.; Huang, Y.; McDonald, A. A comprehensive review of corrosion resistance of thermally-sprayed and thermally-diffused protective coatings on steel structures. *J. Therm. Spray Technol.* **2019**, *28*, 645–677. [[CrossRef](#)]
12. Meghwal, A.; Anupam, A.; Murty, B.; Berndt, C.C.; Kottada, R.S.; Ang, A.S.M. Thermal spray high-entropy alloy coatings: A review. *J. Therm. Spray Technol.* **2020**, *29*, 857–893. [[CrossRef](#)]
13. Li, J.; Huang, Y.; Meng, X.; Xie, Y. A review on high entropy alloys coatings: Fabrication processes and property assessment. *Adv. Eng. Mater.* **2019**, *21*, 1900343. [[CrossRef](#)]

14. Löbel, M.; Lindner, T.; Kohrt, C.; Lampke, T. Processing of AlCoCrFeNiTi high entropy alloy by atmospheric plasma spraying. In Proceedings of the IOP Conference Series: Materials Science and Engineering, Chemnitz, Germany, 16–17 March 2017; p. 012015. [\[CrossRef\]](#)
15. Tian, L.; Feng, Z.; Xiong, W. Microstructure, microhardness, and wear resistance of AlCoCrFeNiTi/Ni60 coating by plasma spraying. *Coatings* **2018**, *8*, 112. [\[CrossRef\]](#)
16. Tian, L.-H.; Xiong, W.; Liu, C.; Lu, S.; Fu, M. Microstructure and wear behavior of atmospheric plasma-sprayed AlCoCrFeNiTi high-entropy alloy coating. *J. Mater. Eng. Perform.* **2016**, *25*, 5513–5521. [\[CrossRef\]](#)
17. Zhu, B.; Alavi, S.; Cheng, C.; Sun, H.; Zhao, H.; Kim, K.S.; Mostaghimi, J.; Zou, Y. Fast and High-Throughput Synthesis of Medium-and High-Entropy Alloys Using Radio Frequency Inductively Coupled Plasma. *Adv. Eng. Mater.* **2021**, *23*, 2001116. [\[CrossRef\]](#)
18. Tu, R.; Li, N.; Li, Q.; Zhang, S.; Zhang, L.; Goto, T. Microstructure and mechanical properties of B4C–HfB2–SiC ternary eutectic composites prepared by arc melting. *J. Eur. Ceram. Soc.* **2016**, *36*, 959–966. [\[CrossRef\]](#)
19. Cedillos-Barraza, O.; Manara, D.; Boboridis, K.; Watkins, T.; Grasso, S.; Jayaseelan, D.D.; Konings, R.J.; Reece, M.J.; Lee, W.E. Investigating the highest melting temperature materials: A laser melting study of the TaC–HfC system. *Sci. Rep.* **2016**, *6*, 37962. [\[CrossRef\]](#) [\[PubMed\]](#)
20. Ang, A.S.M.; Berndt, C.C.; Sesso, M.L.; Anupam, A.; Praveen, S.; Kottada, R.S.; Murty, B. Plasma-sprayed high entropy alloys: Microstructure and properties of AlCoCrFeNi and MnCoCrFeNi. *Metall. Mater. Trans. A* **2015**, *46*, 791–800. [\[CrossRef\]](#)
21. Davis, J. *Handbook of Thermal Spray Technology*, 1st ed.; ASM International, Materials Park: Geauga, OH, USA, 2004; Volume 6994, pp. 1–14.
22. Sharma, A. High Entropy Alloy Coatings and Technology. *Coatings* **2021**, *11*, 372. [\[CrossRef\]](#)
23. Smith, R.W.; Knight, R. Thermal spraying I: Powder consolidation—From coating to forming. *JOM* **1995**, *47*, 32–39. [\[CrossRef\]](#)
24. Bengtsson, P.; Johannesson, T. Characterization of microstructural defects in plasma-sprayed thermal barrier coatings. *J. Therm. Spray Technol.* **1995**, *4*, 245–251. [\[CrossRef\]](#)
25. Huang, R.; Fukanuma, H. Study of the influence of particle velocity on adhesive strength of cold spray deposits. *J. Therm. Spray Technol.* **2012**, *21*, 541–549. [\[CrossRef\]](#)
26. Di Girolamo, G.; Alfano, M.; Pagnotta, L.; Taurino, A.; Zekonyte, J.; Wood, R. On the early stage isothermal oxidation of APS CoNiCrAlY coatings. *J. Mater. Eng. Perform.* **2012**, *21*, 1989–1997. [\[CrossRef\]](#)
27. Planche, M.; Liao, H.; Coddet, C. Oxidation control in atmospheric plasma spraying coating. *Surf. Coat. Technol.* **2007**, *202*, 69–76. [\[CrossRef\]](#)
28. Wei, Q.; Yin, Z.; Li, H. Oxidation control in plasma spraying NiCrCoAlY coating. *Appl. Surf. Sci.* **2012**, *258*, 5094–5099. [\[CrossRef\]](#)
29. Hsu, W.-L.; Murakami, H.; Yeh, J.-W.; Yeh, A.-C.; Shimoda, K. On the study of thermal-sprayed Ni<sub>0.2</sub>Co<sub>0.6</sub>Fe<sub>0.2</sub>CrSi<sub>0.2</sub>AlTi<sub>0.2</sub> HEA overlay coating. *Surf. Coat. Technol.* **2017**, *316*, 71–74. [\[CrossRef\]](#)
30. Alcalá, J.; Gaudette, F.; Suresh, S.; Sampath, S. Instrumented spherical micro-indentation of plasma-sprayed coatings. *Mater. Sci. Eng. A* **2001**, *316*, 1–10. [\[CrossRef\]](#)
31. Neiser, R.; Smith, M.; Dykhuizen, R. Oxidation in wire HVOF-sprayed steel. *J. Therm. Spray Technol.* **1998**, *7*, 537–545. [\[CrossRef\]](#)
32. Mauer, G.; Vaßen, R.; Stöver, D. Plasma and particle temperature measurements in thermal spray: Approaches and applications. *J. Therm. Spray Technol.* **2011**, *20*, 391–406. [\[CrossRef\]](#)
33. Gludovatz, B.; Hohenwarter, A.; Catoor, D.; Chang, E.H.; George, E.P.; Ritchie, R.O. A fracture-resistant high-entropy alloy for cryogenic applications. *Science* **2014**, *345*, 1153–1158. [\[CrossRef\]](#)
34. Anupam, A.; Kottada, R.S.; Kashyap, S.; Meghwal, A.; Murty, B.; Berndt, C.; Ang, A. Understanding the microstructural evolution of high entropy alloy coatings manufactured by atmospheric plasma spray processing. *Appl. Surf. Sci.* **2020**, *505*, 144117. [\[CrossRef\]](#)
35. Shi, P.; Yu, Y.; Xiong, N.; Liu, M.; Qiao, Z.; Yi, G.; Yao, Q.; Zhao, G.; Xie, E.; Wang, Q. Microstructure and tribological behavior of a novel atmospheric plasma sprayed AlCoCrFeNi high entropy alloy matrix self-lubricating composite coatings. *Tribol. Int.* **2020**, *151*, 106470. [\[CrossRef\]](#)
36. Lehtonen, J.; Koivuluoto, H.; Ge, Y.; Juselius, A.; Hannula, S.-P. Cold gas spraying of a high-entropy CrFeNiMn equiatomic alloy. *Coatings* **2020**, *10*, 53. [\[CrossRef\]](#)
37. Anupam, A.; Kumar, S.; Chavan, N.M.; Murty, B.S.; Kottada, R.S. First report on cold-sprayed AlCoCrFeNi high-entropy alloy and its isothermal oxidation. *J. Mater. Res.* **2019**, *34*, 796–806. [\[CrossRef\]](#)
38. Yin, S.; Li, W.; Song, B.; Yan, X.; Kuang, M.; Xu, Y.; Wen, K.; Lupoi, R. Deposition of FeCoNiCrMn high entropy alloy (HEA) coating via cold spraying. *J. Mater. Sci. Technol.* **2019**, *35*, 1003–1007. [\[CrossRef\]](#)
39. Matthews, S. Shrouded plasma spray of Ni–20Cr coatings utilizing internal shroud film cooling. *Surf. Coat. Technol.* **2014**, *249*, 56–74. [\[CrossRef\]](#)
40. Morks, M.; Berndt, C. Corrosion and oxidation properties of NiCr coatings sprayed in presence of gas shroud system. *Appl. Surf. Sci.* **2010**, *256*, 4322–4327. [\[CrossRef\]](#)
41. Salhi, Z.; Klein, D.; Gougeon, P.; Coddet, C. Development of coating by thermal plasma spraying under very low-pressure condition <1 mbar. *Vacuum* **2005**, *77*, 145–150. [\[CrossRef\]](#)
42. Wang, C.; Yu, J.; Zhang, Y.; Yu, Y. Phase evolution and solidification cracking sensibility in laser remelting treatment of the plasma-sprayed CrMnFeCoNi high entropy alloy coating. *Mater. Des.* **2019**, *182*, 108040. [\[CrossRef\]](#)

43. Nair, R.B.; Ngan, S.; McDonald, A. Dry abrasive wear and solid particle erosion assessments of high entropy alloy coatings fabricated by cold spraying. *Mater. Today. Commun.* **2023**, *34*, 105527. [[CrossRef](#)]
44. Meghwal, A.; Anupam, A.; Schulz, C.; Hall, C.; Murty, B.S.; Kottada, R.S.; Vijay, R.; Munroe, P.; Berndt, C.C.; Ang, A.S.M. Tribological and corrosion performance of an atmospheric plasma sprayed AlCoCr0.5Ni high-entropy alloy coating. *Wear* **2022**, *506*, 204443. [[CrossRef](#)]
45. Pal, S.; Nair, R.B.; McDonald, A. Toward understanding the microstructure and electrical resistivity of thermal-sprayed high-entropy alloy coatings. *J. Mater. Sci.* **2022**, *57*, 20928–20944. [[CrossRef](#)]
46. Xing, B.; Zuo, X.; Li, Q.; Jin, B.; Zhang, N.; Yin, S. Influence of Microstructure Evolution on the Electrochemical Corrosion Behavior of (CoCrFeNi)<sub>94</sub>Ti<sub>1.5</sub>Al<sub>4.5</sub> High Entropy Alloy Coatings. *J. Therm. Spray Technol.* **2022**, *31*, 1375–1385. [[CrossRef](#)]
47. Yurkova, A.; Hushchyk, D.; Minitzky, A. Synthesis of High-Entropy AlNiCoFeCrTi Coating by Cold Spraying. *Powder Metall. Met. Ceram.* **2021**, *59*, 681–694. [[CrossRef](#)]
48. Ghadami, F.; Davoudabadi, M.A.; Ghadami, S. Cyclic Oxidation Properties of the Nanocrystalline AlCrFeCoNi High-Entropy Alloy Coatings Applied by the Atmospheric Plasma Spraying Technique. *Coatings* **2022**, *12*, 372. [[CrossRef](#)]
49. Huang, P.K.; Yeh, J.W.; Shun, T.T.; Chen, S.K. Multi-principal-element alloys with improved oxidation and wear resistance for thermal spray coating. *Adv. Eng. Mater.* **2004**, *6*, 74–78. [[CrossRef](#)]
50. Tung, C.-C.; Yeh, J.-W.; Shun, T.-T.; Chen, S.-K.; Huang, Y.-S.; Chen, H.-C. On the elemental effect of AlCoCrCuFeNi high-entropy alloy system. *Mater. Lett.* **2007**, *61*, 1–5. [[CrossRef](#)]
51. Cheng, K.-C.; Chen, J.-H.; Stadler, S.; Chen, S.-H. Properties of atomized AlCoCrFeNi high-entropy alloy powders and their phase-adjustable coatings prepared via plasma spray process. *Appl. Surf. Sci.* **2019**, *478*, 478–486. [[CrossRef](#)]
52. Vaidya, M.; Muralikrishna, G.M.; Murty, B.S. High-entropy alloys by mechanical alloying: A review. *J. Mater. Res.* **2019**, *34*, 664–686. [[CrossRef](#)]
53. Yue, T.M.; Xie, H.; Lin, X.; Yang, H.; Meng, G. Microstructure of laser re-melted AlCoCrCuFeNi high entropy alloy coatings produced by plasma spraying. *Entropy* **2013**, *15*, 2833–2845. [[CrossRef](#)]
54. Wang, L.; Chen, C.; Yeh, J.; Ke, S. The microstructure and strengthening mechanism of thermal spray coating Ni<sub>x</sub>Co<sub>0.6</sub>Fe<sub>0.2</sub>CrySizAlTi<sub>0.2</sub> high-entropy alloys. *Mater. Chem. Phys.* **2011**, *126*, 880–885. [[CrossRef](#)]
55. Thirathipviwat, P.; Sato, S.; Song, G.; Bednarcik, J.; Nielsch, K.; Jung, J.; Han, J. A role of atomic size misfit in lattice distortion and solid solution strengthening of TiNbHfTaZr high entropy alloy system. *Scr. Mater.* **2022**, *210*, 114470. [[CrossRef](#)]
56. Wang, L.; Zhang, F.; Yan, S.; Yu, G.; Chen, J.; He, J.; Yin, F. Microstructure evolution and mechanical properties of atmosphere plasma sprayed AlCoCrFeNi high-entropy alloy coatings under post-annealing. *J. Alloys Compd.* **2021**, *872*, 159607. [[CrossRef](#)]
57. Mu, Y.; Zhang, L.; Xu, L.; Prashanth, K.; Zhang, N.; Ma, X.; Jia, Y.; Xu, Y.; Jia, Y.; Wang, G. Frictional wear and corrosion behavior of AlCoCrFeNi high-entropy alloy coatings synthesized by atmospheric plasma spraying. *Entropy* **2020**, *22*, 740. [[CrossRef](#)] [[PubMed](#)]
58. Tian, L.; Fu, M.; Xiong, W. Microstructural Evolution of AlCoCrFeNiSi High-Entropy Alloy Powder during Mechanical Alloying and Its Coating Performance. *Materials* **2018**, *11*, 320. [[CrossRef](#)] [[PubMed](#)]
59. Nair, R.B.; Perumal, G.; McDonald, A. Effect of Microstructure on Wear and Corrosion Performance of Thermally-Sprayed AlCoCrFeMo High Entropy Alloy Coatings. *Adv. Eng. Mater.* **2022**, *24*, 2101713. [[CrossRef](#)]
60. Rojas, D.F.; Li, H.; Orhan, O.K.; Shao, C.; Hogan, J.D.; Ponga, M. Mechanical and microstructural properties of a CoCrFe<sub>0.75</sub>NiMo<sub>0.3</sub>Nb<sub>0.125</sub> high-entropy alloy additively manufactured via cold-spray. *J. Alloys Compd.* **2022**, *893*, 162309. [[CrossRef](#)]
61. Löbel, M.; Lindner, T.; Mehner, T.; Rymer, L.-M.; Lampke, T.; Björklund, S.; Joshi, S. Microstructure and Corrosion Properties of AlCoCrFeNi High-Entropy Alloy Coatings Prepared by HVOF and HVOF. In Proceedings of the Thermal Spray 2021: Proceedings from the International Thermal Spray Conference (ITSC), Quebec City, QC, Canada, 24–28 May 2021; pp. 416–421. [[CrossRef](#)]
62. Wei, Z.; Wu, Y.; Hong, S.; Cheng, J.; Qiao, L.; Cheng, J.; Zhu, S. Ultrasonic cavitation erosion behaviors of high-velocity oxygen-fuel (HVOF) sprayed AlCoCrFeNi high-entropy alloy coating in different solutions. *Surf. Coat. Technol.* **2021**, *409*, 126899. [[CrossRef](#)]
63. Liao, W.-B.; Wu, Z.-X.; Lu, W.; He, M.; Wang, T.; Guo, Z.; Huang, J. Microstructures and mechanical properties of CoCrFeNiMn high-entropy alloy coatings by detonation spraying. *Intermetallics* **2021**, *132*, 107138. [[CrossRef](#)]
64. He, F.; Wang, Z.; Wu, Q.; Li, J.; Wang, J.; Liu, C. Phase separation of metastable CoCrFeNi high entropy alloy at intermediate temperatures. *Scr. Mater.* **2017**, *126*, 15–19. [[CrossRef](#)]
65. Rogachev, A.; Vadchenko, S.; Kochetov, N.; Rouvimov, S.; Kovalev, D.Y.; Shchukin, A.; Moskovskikh, D.; Nepapushev, A.; Mukasyan, A. Structure and properties of equiatomic CoCrFeNiMn alloy fabricated by high-energy ball milling and spark plasma sintering. *J. Alloys Compd.* **2019**, *805*, 1237–1245. [[CrossRef](#)]
66. Mahdavi, A.; Pourasghar, A.; Chen, Z.; McDonald, A. Particle–Substrate Transient Thermal Evolution During Cold Spray Deposition Process: A Hybrid Heat Conduction Analysis. *J. Therm. Spray Technol.* **2020**, *29*, 1609–1627. [[CrossRef](#)]
67. Lee, Y.T.R.; Ashrafzadeh, H.; Fisher, G.; McDonald, A. Effect of type of reinforcing particles on the deposition efficiency and wear resistance of low-pressure cold-sprayed metal matrix composite coatings. *Surf. Coat. Technol.* **2017**, *324*, 190–200. [[CrossRef](#)]
68. Meghwal, A.; Anupam, A.; Luzin, V.; Schulz, C.; Hall, C.; Murty, B.S.; Kottada, R.S.; Berndt, C.C.; Ang, A.S.M. Multiscale mechanical performance and corrosion behaviour of plasma sprayed AlCoCrFeNi high-entropy alloy coatings. *J. Alloys Compd.* **2021**, *854*, 157140. [[CrossRef](#)]

69. Li, H.; Li, J.; Yan, C.; Zhang, X.; Xiong, D. Microstructure and Tribological Properties of Plasma-Sprayed Al<sub>0.2</sub>Co<sub>1.5</sub>CrFeNi<sub>1.5</sub>Ti-Ag Composite Coating from 25 to 750 °C. *J. Mater. Eng. Perform.* **2020**, *29*, 1640–1649. [[CrossRef](#)]
70. Li, T.; Liu, Y.; Liu, B.; Guo, W.; Xu, L. Microstructure and Wear Behavior of FeCoCrNiMo<sub>0.2</sub> High Entropy Coatings Prepared by Air Plasma Spray and the High Velocity Oxy-Fuel Spray Processes. *Coatings* **2017**, *7*, 151. [[CrossRef](#)]
71. Shun, T.-T.; Chang, L.-Y.; Shiu, M.-H. Microstructure and mechanical properties of multiprincipal component CoCrFeNiMox alloys. *Mater. Charact.* **2012**, *70*, 63–67. [[CrossRef](#)]
72. Wei, Z.; Wu, Y.; Hong, S.; Cheng, J.; Qiao, L.; Cheng, J.; Zhu, S. Effect of WC-10Co on cavitation erosion behaviors of AlCoCrFeNi coatings prepared by HVOF spraying. *Ceram. Int.* **2021**, *47*, 15121–15128. [[CrossRef](#)]
73. Wu, H.; Huang, S.; Zhu, H.; Xie, Z. Strengthening FeCrNiCu high entropy alloys via combining V additions with in-situ TiC particles. *Scr. Mater.* **2021**, *195*, 113724. [[CrossRef](#)]
74. Zhu, S.; Zhang, Z.; Zhang, B.; Yu, Y.; Wang, Z.; Zhang, X.; Lu, B. Microstructure and Properties of Al<sub>2</sub>O<sub>3</sub>-13wt.%TiO<sub>2</sub>-Reinforced CoCrFeMnNi High-Entropy Alloy Composite Coatings Prepared by Plasma Spraying. *J. Therm. Spray Technol.* **2021**, *30*, 772–786. [[CrossRef](#)]
75. Dieter, G.E.; Bacon, D.J. *Mechanical Metallurgy*; McGraw-Hill: New York, NY, USA, 1976; Volume 3.
76. Deng, K.-K.; Wang, X.-J.; Wang, C.-J.; Shi, J.-Y.; Hu, X.-S.; Wu, K. Effects of bimodal size SiC particles on the microstructure evolution and fracture mechanism of AZ91 matrix at room temperature. *Mater. Sci. Eng. A* **2012**, *553*, 74–79. [[CrossRef](#)]
77. Jin, B.; Zhang, N.; Guan, S.; Zhang, Y.; Li, D. Microstructure and properties of laser re-melting FeCoCrNiAl<sub>0.5</sub>Si<sub>x</sub> high-entropy alloy coatings. *Surf. Coat. Technol.* **2018**, *349*, 867–873. [[CrossRef](#)]
78. Löbel, M.; Lindner, T.; Mehner, T.; Lampke, T. Microstructure and wear resistance of AlCoCrFeNiTi high-entropy alloy coatings produced by HVOF. *Coatings* **2017**, *7*, 144. [[CrossRef](#)]
79. Chen, L.; Bobzin, K.; Zhou, Z.; Zhao, L.; Öte, M.; Königstein, T.; Tan, Z.; He, D. Wear behavior of HVOF-sprayed Al<sub>0.6</sub>TiCrFeCoNi high entropy alloy coatings at different temperatures. *Surf. Coat. Technol.* **2019**, *358*, 215–222. [[CrossRef](#)]
80. Munday, G.; Hogan, J.; McDonald, A. On the microstructure-dependency of mechanical properties and failure of low-pressure cold-sprayed tungsten carbide-nickel metal matrix composite coatings. *Surf. Coat. Technol.* **2020**, *396*, 125947. [[CrossRef](#)]
81. Zhuang, W.Z.; Halford, G.R. Investigation of residual stress relaxation under cyclic load. *Int. J. Fatigue* **2001**, *23*, 31–37. [[CrossRef](#)]
82. McGrann, R.; Greving, D.; Shadley, J.; Rybicki, E.F.; Kruecke, T.; Bodger, B. The effect of coating residual stress on the fatigue life of thermal spray-coated steel and aluminum. *Surf. Coat. Technol.* **1998**, *108*, 59–64. [[CrossRef](#)]
83. Oka, Y.; Ohnogi, H.; Hosokawa, T.; Matsumura, M. The impact angle dependence of erosion damage caused by solid particle impact. *Wear* **1997**, *203*, 573–579. [[CrossRef](#)]
84. Oka, Y.; Mihara, S.; Yoshida, T. Impact-angle dependence and estimation of erosion damage to ceramic materials caused by solid particle impact. *Wear* **2009**, *267*, 129–135. [[CrossRef](#)]
85. Grewal, H.S.; Nair, R.B.; Arora, H.S. Complex concentrated alloy bimodal composite claddings with enhanced cavitation erosion resistance. *Surf. Coat. Technol.* **2020**, *392*, 125751. [[CrossRef](#)]
86. Nair, R.B.; Arora, H.S.; Grewal, H.S. Slurry erosion–corrosion of bimodal complex concentrated alloy composite cladding. *Adv. Eng. Mater.* **2020**, *22*, 2000626. [[CrossRef](#)]
87. Nair, R.B.; Arora, H.S.; Boyana, A.V.; Saiteja, P.; Grewal, H.S. Tribological behavior of microwave synthesized high entropy alloy claddings. *Wear* **2019**, *436*, 203028. [[CrossRef](#)]
88. Sexsmith, M.; Troczynski, T. Peel adhesion test for thermal spray coatings. *J. Therm. Spray Technol.* **1994**, *3*, 404–411. [[CrossRef](#)]
89. Amada, S.; Hirose, T. Influence of grit blasting pre-treatment on the adhesion strength of plasma sprayed coatings: Fractal analysis of roughness. *Surf. Coat. Technol.* **1998**, *102*, 132–137. [[CrossRef](#)]
90. Bolis, C.; Berthe, L.; Boustie, M.; Arrigoni, M.; Barradas, S.; Jeandin, M. Physical approach to adhesion testing using laser-driven shock waves. *J. Phys. D Appl. Phys.* **2007**, *40*, 3155. [[CrossRef](#)]
91. Barradas, S.; Molins, R.; Jeandin, M.; Arrigoni, M.; Boustie, M.; Bolis, C.; Berthe, L.; Ducos, M. Application of laser shock adhesion testing to the study of the interlamellar strength and coating–substrate adhesion in cold-sprayed copper coating of aluminum. *Surf. Coat. Technol.* **2005**, *197*, 18–27. [[CrossRef](#)]
92. Beydon, R.; Bernhart, G.; Segui, Y. Measurement of metallic coatings adhesion to fibre reinforced plastic materials. *Surf. Coat. Technol.* **2000**, *126*, 39–47. [[CrossRef](#)]
93. Löbel, M.; Lindner, T.; Lampke, T. High-temperature wear behaviour of AlCoCrFeNiTi<sub>0.5</sub> coatings produced by HVOF. *Surf. Coat. Technol.* **2020**, *403*, 126379. [[CrossRef](#)]
94. Patel, P.; Alidokht, S.A.; Sharifi, N.; Roy, A.; Harrington, K.; Stoyanov, P.; Chromik, R.R.; Moreau, C. Microstructural and Tribological Behavior of Thermal Spray CrMnFeCoNi High Entropy Alloy Coatings. *J. Therm. Spray Technol.* **2022**, *31*, 1285–1301. [[CrossRef](#)]
95. Supekar, R.; Nair, R.B.; McDonald, A.; Stoyanov, P. Sliding wear behavior of high entropy alloy coatings deposited through cold spraying and flame spraying: A comparative assessment. *Wear* **2023**, *516*, 204596. [[CrossRef](#)]
96. Silvello, A.; Cavaliere, P.; Yin, S.; Lupoi, R.; Garcia Cano, I.; Dosta, S. Microstructural, Mechanical and Wear Behavior of HVOF and Cold-Sprayed High-Entropy Alloys (HEAs) Coatings. *J. Therm. Spray Technol.* **2022**, *31*, 1184–1206. [[CrossRef](#)]
97. Nair, R.; Arora, H.; Mukherjee, S.; Singh, S.; Singh, H.; Grewal, H. Exceptionally high cavitation erosion and corrosion resistance of a high entropy alloy. *Ultrason. Sonochem.* **2018**, *41*, 252–260. [[CrossRef](#)] [[PubMed](#)]
98. Shi, Y.; Yang, B.; Liaw, P.K. Corrosion-resistant high-entropy alloys: A review. *Metals* **2017**, *7*, 43. [[CrossRef](#)]

99. Wang, W.; Qi, W.; Xie, L.; Yang, X.; Li, J.; Zhang, Y. Microstructure and corrosion behavior of (CoCrFeNi)<sub>95</sub>Nb<sub>5</sub> high-entropy alloy coating fabricated by plasma spraying. *Materials* **2019**, *12*, 694. [[CrossRef](#)] [[PubMed](#)]
100. Vallimanalan, A.; Kumares Babu, S.P.; Muthukumar, S.; Murali, M.; Gaurav, V.; Mahendran, R. Corrosion behaviour of thermally sprayed Mo added AlCoCrNi high entropy alloy coating. *Mater. Today Proc.* **2020**, *27*, 2398–2400. [[CrossRef](#)]
101. Liu, S.; Peng, Y.; Zhang, Y.; Wang, Y.; Fan, W.; Wang, A.; Zhang, W.; Tan, Y.; Ma, Q.; Lan, Y. Effect of Nanostructure on Wear and Corrosion Behavior of HVAF-Sprayed Eutectic High-Entropy Alloy Coatings. *J. Therm. Spray Technol.* **2022**, *31*, 1252–1262. [[CrossRef](#)]
102. Fan, Q.; Chen, C.; Fan, C.; Liu, Z.; Cai, X.; Lin, S.; Yang, C. AlCoCrFeNi high-entropy alloy coatings prepared by gas tungsten arc cladding: Microstructure, mechanical and corrosion properties. *Intermetallics* **2021**, *138*, 107337. [[CrossRef](#)]
103. Aliyu, A.; Srivastava, C. Microstructure-corrosion property correlation in electrodeposited AlCrFeCoNiCu high entropy alloys-graphene oxide composite coatings. *Thin Solid Films* **2019**, *686*, 137434. [[CrossRef](#)]
104. Qiu, X.-W.; Liu, C.-G. Microstructure and properties of Al<sub>2</sub>CrFeCoCuTiNi<sub>x</sub> high-entropy alloys prepared by laser cladding. *J. Alloys Compd.* **2013**, *553*, 216–220. [[CrossRef](#)]
105. Wang, J.; Chen, Y.; Zhang, Y.; Dai, W.; Xu, Q.; Li, W.; Liu, Y. Corrosion and slurry erosion wear performances of coaxial direct laser deposited CoCrFeNiCu<sub>1-x</sub>Mox high-entropy coatings by modulating the second-phase precipitation. *Mater. Des.* **2021**, *212*, 110277. [[CrossRef](#)]
106. Hsu, W.-L.; Murakami, H.; Araki, H.; Watanabe, M.; Kuroda, S.; Yeh, A.-C.; Yeh, J.-W. A Study of NiCo<sub>0.6</sub>Fe<sub>0.2</sub>Cr<sub>x</sub>SiAlTi<sub>y</sub>High-Entropy Alloys for Applications as a High-Temperature Protective Coating and a Bond Coat in Thermal Barrier Coating Systems. *J. Electrochem. Soc.* **2018**, *165*, C524–C531. [[CrossRef](#)]
107. Hsu, W.-L.; Yang, Y.-C.; Chen, C.-Y.; Yeh, J.-W. Thermal sprayed high-entropy NiCo<sub>0.6</sub>Fe<sub>0.2</sub>Cr<sub>1.5</sub>SiAlTi<sub>0.2</sub> coating with improved mechanical properties and oxidation resistance. *Intermetallics* **2017**, *89*, 105–110. [[CrossRef](#)]
108. Xu, Y.; Li, W.; Qu, L.; Yang, X.; Song, B.; Lupoi, R.; Yin, S. Solid-state cold spraying of FeCoCrNiMn high-entropy alloy: An insight into microstructure evolution and oxidation behavior at 700–900 °C. *J. Mater. Sci. Technol.* **2021**, *68*, 172–183. [[CrossRef](#)]
109. Senkov, O.; Wilks, G.; Miracle, D.; Chuang, C.; Liaw, P. Refractory high-entropy alloys. *Intermetallics* **2010**, *18*, 1758–1765. [[CrossRef](#)]
110. Liu, C.; Wang, H.; Zhang, S.; Tang, H.; Zhang, A. Microstructure and oxidation behavior of new refractory high entropy alloys. *J. Alloys Compd.* **2014**, *583*, 162–169. [[CrossRef](#)]
111. Senkov, O.N.; Miracle, D.B.; Chaput, K.J.; Couzinie, J.-P. Development and exploration of refractory high entropy alloys—A review. *J. Mater. Res.* **2018**, *33*, 3092–3128. [[CrossRef](#)]
112. Gorr, B.; Azim, M.; Christ, H.-J.; Mueller, T.; Schliephake, D.; Heilmaier, M. Phase equilibria, microstructure, and high temperature oxidation resistance of novel refractory high-entropy alloys. *J. Alloys Compd.* **2015**, *624*, 270–278. [[CrossRef](#)]
113. Gorr, B.; Müller, F.; Azim, M.; Christ, H.-J.; Müller, T.; Chen, H.; Kauffmann, A.; Heilmaier, M. High-temperature oxidation behavior of refractory high-entropy alloys: Effect of alloy composition. *Oxid. Met.* **2017**, *88*, 339–349. [[CrossRef](#)]
114. Müller, F.; Gorr, B.; Christ, H.-J.; Müller, J.; Butz, B.; Chen, H.; Kauffmann, A.; Heilmaier, M. On the oxidation mechanism of refractory high entropy alloys. *Corros. Sci.* **2019**, *159*, 108161. [[CrossRef](#)]
115. Gorr, B.; Mueller, F.; Christ, H.-J.; Mueller, T.; Chen, H.; Kauffmann, A.; Heilmaier, M. High temperature oxidation behavior of an equimolar refractory metal-based alloy 20Nb20Mo20Cr20Ti20Al with and without Si addition. *J. Alloys Compd.* **2016**, *688*, 468–477. [[CrossRef](#)]
116. Gorr, B.; Mueller, F.; Christ, H.-J.; Chen, H.; Kauffmann, A.; Schweiger, R.; Szabó, D.V.; Heilmaier, M. Development of Oxidation Resistant Refractory High Entropy Alloys for High Temperature Applications: Recent Results and Development Strategy. In Proceedings of the TMS Annual Meeting & Exhibition, Phoenix, AZ, USA, 11–15 March 2018; pp. 647–659.
117. Gorr, B.; Azim, M.; Christ, H.-J.; Chen, H.; Szabo, D.V.; Kauffmann, A.; Heilmaier, M. Microstructure evolution in a new refractory high-entropy alloy W-Mo-Cr-Ti-Al. *Metall. Mater. Trans. A* **2016**, *47*, 961–970. [[CrossRef](#)]
118. Stoyanov, P.; Harrington, K.M.; Frye, A. Insights into the Tribological Characteristic of Cu-Based Coatings Under Extreme Contact Conditions. *JOM* **2020**, *72*, 2191–2197. [[CrossRef](#)]
119. Chupp, R.E.; Hendricks, R.C.; Lattime, S.B.; Steinetz, B.M. Sealing in Turbomachinery. *J. Propuls. Power* **2006**, *22*, 313–349. [[CrossRef](#)]
120. Lim, K.R.; Lee, K.S.; Lee, J.S.; Kim, J.Y.; Chang, H.J.; Na, Y.S. Dual-phase high-entropy alloys for high-temperature structural applications. *J. Alloys Compd.* **2017**, *728*, 1235–1238. [[CrossRef](#)]
121. Grewal, H.S.; Sanjiv, R.M.; Arora, H.S.; Kumar, R.; Ayyagari, A.; Mukherjee, S.; Singh, H. Activation Energy and High Temperature Oxidation Behavior of Multi-Principal Element Alloy. *Adv. Eng. Mater.* **2017**, *19*, 1700182. [[CrossRef](#)]
122. Zhou, J.; Zhang, J.; Zhang, F.; Niu, B.; Lei, L.; Wang, W. High-entropy carbide: A novel class of multicomponent ceramics. *Ceram. Int.* **2018**, *44*, 22014–22018. [[CrossRef](#)]
123. Harrington, T.J.; Gild, J.; Sarker, P.; Toher, C.; Rost, C.M.; Diplo, O.F.; McElfresh, C.; Kaufmann, K.; Marin, E.; Borowski, L.; et al. Phase stability and mechanical properties of novel high entropy transition metal carbides. *Acta Mater.* **2019**, *166*, 271–280. [[CrossRef](#)]
124. Liu, D.; Zhang, A.; Jia, J.; Meng, J.; Su, B. Phase evolution and properties of (VNbTaMoW)C high entropy carbide prepared by reaction synthesis. *J. Eur. Ceram. Soc.* **2020**, *40*, 2746–2751. [[CrossRef](#)]

125. Wang, Y.; Csanádi, T.; Zhang, H.; Dusza, J.; Reece, M.J.; Zhang, R.Z. Enhanced Hardness in High-Entropy Carbides through Atomic Randomness. *Adv. Theory Simul.* **2020**, *3*, 2000111. [[CrossRef](#)]
126. Musicó, B.L.; Gilbert, D.; Ward, T.Z.; Page, K.; George, E.; Yan, J.; Mandrus, D.; Keppens, V. The emergent field of high entropy oxides: Design, prospects, challenges, and opportunities for tailoring material properties. *APL Mater.* **2020**, *8*, 040912. [[CrossRef](#)]
127. Witte, R.; Sarkar, A.; Kruk, R.; Eggert, B.; Brand, R.A.; Wende, H.; Hahn, H. High-entropy oxides: An emerging prospect for magnetic rare-earth transition metal perovskites. *Phys. Rev. Mater.* **2019**, *3*, 034406. [[CrossRef](#)]
128. Mao, A.; Xiang, H.-Z.; Zhang, Z.-G.; Kuramoto, K.; Zhang, H.; Jia, Y. A new class of spinel high-entropy oxides with controllable magnetic properties. *J. Magn. Magn. Mater.* **2020**, *497*, 165884. [[CrossRef](#)]
129. Wang, Q.; Sarkar, A.; Li, Z.; Lu, Y.; Velasco, L.; Bhattacharya, S.S.; Brezesinski, T.; Hahn, H.; Breitung, B. High entropy oxides as anode material for Li-ion battery applications: A practical approach. *Electrochem. Commun.* **2019**, *100*, 121–125. [[CrossRef](#)]
130. Albedwawi, S.H.; Aljaberi, A.; Haidemenopoulos, G.N.; Polychronopoulou, K. High entropy oxides-exploring a paradigm of promising catalysts: A review. *Mater. Des.* **2021**, *202*, 109534. [[CrossRef](#)]
131. Zhou, S.; Pu, Y.; Zhang, Q.; Shi, R.; Guo, X.; Wang, W.; Ji, J.; Wei, T.; Ouyang, T. Microstructure and dielectric properties of high entropy Ba(Zr<sub>0.2</sub>Ti<sub>0.2</sub>Sn<sub>0.2</sub>Hf<sub>0.2</sub>Me<sub>0.2</sub>)O<sub>3</sub> perovskite oxides. *Ceram. Int.* **2020**, *46*, 7430–7437. [[CrossRef](#)]
132. Sarkar, A.; Velasco, L.; Wang, D.; Wang, Q.; Talasila, G.; de Biasi, L.; Kübel, C.; Brezesinski, T.; Bhattacharya, S.S.; Hahn, H.; et al. High entropy oxides for reversible energy storage. *Nat. Commun.* **2018**, *9*, 3400. [[CrossRef](#)]
133. Dehaghani, S.T.; Dolatabadi, A.; McDonald, A. Thermally sprayed metal matrix composite coatings as heating systems. *Appl. Therm. Eng.* **2021**, *196*, 117321. [[CrossRef](#)]
134. Clyne, T.W.; Withers, P.J. *An Introduction to Metal Matrix Composites*; Cambridge University Press: Cambridge, UK, 1993.
135. Riva, S.; Tudball, A.; Mehraban, S.; Lavery, N.P.; Brown, S.G.R.; Yussenko, K.V. A novel High-Entropy Alloy-based composite material. *J. Alloys Compd.* **2018**, *730*, 544–551. [[CrossRef](#)]
136. Zhu, S.; Yu, Y.; Zhang, B.; Zhang, Z.; Yan, X.; Wang, Z. Microstructure and wear behaviour of in-situ TiN-Al<sub>2</sub>O<sub>3</sub> reinforced CoCrFeNiMn high-entropy alloys composite coatings fabricated by plasma cladding. *Mater. Lett.* **2020**, *272*, 127870. [[CrossRef](#)]
137. Fan, Q.C.; Li, B.S.; Zhang, Y. The microstructure and properties of (FeCrNiCo)AlxCu<sub>y</sub> high-entropy alloys and their TiC-reinforced composites. *Mater. Sci. Eng. A* **2014**, *598*, 244–250. [[CrossRef](#)]
138. Colombini, E.; Lassinantti Gualtieri, M.; Rosa, R.; Tarterini, F.; Zadra, M.; Casagrande, A.; Veronesi, P. SPS-assisted Synthesis of SiCp reinforced high entropy alloys: Reactivity of SiC and effects of pre-mechanical alloying and post-annealing treatment. *Powder Metall.* **2018**, *61*, 64–72. [[CrossRef](#)]
139. Li, Z.; Liu, X.; Guo, K.; Wang, H.; Cai, B.; Chang, F.; Hong, C.; Dai, P. Microstructure and properties of Ti(C, N)–TiB<sub>2</sub>–FeCoCrNiAl high-entropy alloys composite cermets. *Mater. Sci. Eng. A* **2019**, *767*, 138427. [[CrossRef](#)]
140. Karthik, G.M.; Panikar, S.; Ram, G.D.J.; Kottada, R.S. Additive manufacturing of an aluminum matrix composite reinforced with nanocrystalline high-entropy alloy particles. *Mater. Sci. Eng. A* **2017**, *679*, 193–203. [[CrossRef](#)]
141. Amar, A.; Li, J.; Xiang, S.; Liu, X.; Zhou, Y.; Le, G.; Wang, X.; Qu, F.; Ma, S.; Dong, W. Additive manufacturing of high-strength CrMnFeCoNi-based High Entropy Alloys with TiC addition. *Intermetallics* **2019**, *109*, 162–166. [[CrossRef](#)]
142. Todai, M.; Nagase, T.; Hori, T.; Matsugaki, A.; Sekita, A.; Nakano, T. Novel TiNbTaZrMo high-entropy alloys for metallic biomaterials. *Scr. Mater.* **2017**, *129*, 65–68. [[CrossRef](#)]
143. Hori, T.; Nagase, T.; Todai, M.; Matsugaki, A.; Nakano, T. Development of non-equiatomic Ti-Nb-Ta-Zr-Mo high-entropy alloys for metallic biomaterials. *Scr. Mater.* **2019**, *172*, 83–87. [[CrossRef](#)]
144. Nagase, T.; Iijima, Y.; Matsugaki, A.; Ameyama, K.; Nakano, T. Design and fabrication of Ti–Zr–Hf–Cr–Mo and Ti–Zr–Hf–Co–Cr–Mo high-entropy alloys as metallic biomaterials. *Mater. Sci. Eng. C* **2020**, *107*, 110322. [[CrossRef](#)]
145. Castro, D.; Jaeger, P.; Baptista, A.C.; Oliveira, J.P. An overview of high-entropy alloys as biomaterials. *Metals* **2021**, *11*, 648. [[CrossRef](#)]
146. Gurel, S.; Nazarahari, A.; Canadinc, D.; Cabuk, H.; Bal, B. Assessment of biocompatibility of novel TiTaHf-based high entropy alloys for utility in orthopedic implants. *Mater. Chem. Phys.* **2021**, *266*, 124573. [[CrossRef](#)]
147. Perumal, G.; Grewal, H.S.; Pole, M.; Reddy, L.V.K.; Mukherjee, S.; Singh, H.; Manivasagam, G.; Arora, H.S. Enhanced biocorrosion resistance and cellular response of a dual-phase high entropy alloy through reduced elemental heterogeneity. *ACS Appl. Bio Mater.* **2020**, *3*, 1233–1244. [[CrossRef](#)]
148. Shittu, J.; Pole, M.; Cockerill, I.; Sadeghilaridjani, M.; Reddy, L.V.K.; Manivasagam, G.; Singh, H.; Grewal, H.S.; Arora, H.S.; Mukherjee, S. Biocompatible High Entropy Alloys with Excellent Degradation Resistance in a Simulated Physiological Environment. *ACS Appl. Bio Mater.* **2020**, *3*, 8890–8900. [[CrossRef](#)]
149. Cusentino, M.; Wood, M.; Dingreville, R. Compositional and structural origins of radiation damage mitigation in high-entropy alloys. *J. Appl. Phys.* **2020**, *128*, 125904. [[CrossRef](#)]
150. Patel, D.; Richardson, M.D.; Jim, B.; Akhmaliev, S.; Goodall, R.; Gandy, A.S. Radiation damage tolerance of a novel metastable refractory high entropy alloy V<sub>2.5</sub>Cr<sub>1.2</sub>WMoCo<sub>0.04</sub>. *J. Nucl. Mater.* **2020**, *531*, 152005. [[CrossRef](#)]

151. Guo, L.; Gu, J.; Gong, X.; Ni, S.; Song, M. CALPHAD aided design of high entropy alloy to achieve high strength via precipitate strengthening. *Sci. China Mater.* **2020**, *63*, 288–299. [[CrossRef](#)]
152. Xiao, J.-K.; Tan, H.; Wu, Y.-Q.; Chen, J.; Zhang, C. Microstructure and wear behavior of FeCoNiCrMn high entropy alloy coating deposited by plasma spraying. *Surf. Coat. Technol.* **2020**, *385*, 125430. [[CrossRef](#)]

**Disclaimer/Publisher’s Note:** The statements, opinions and data contained in all publications are solely those of the individual author(s) and contributor(s) and not of MDPI and/or the editor(s). MDPI and/or the editor(s) disclaim responsibility for any injury to people or property resulting from any ideas, methods, instructions or products referred to in the content.